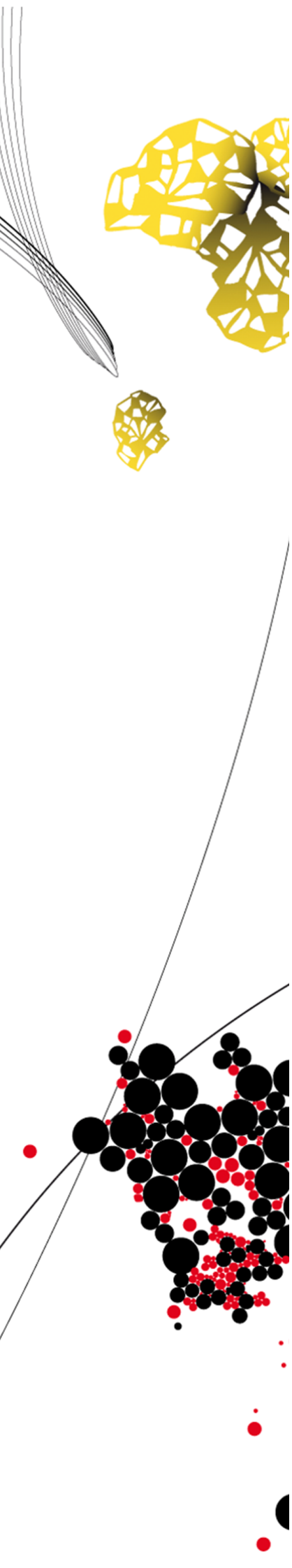

UNIVERSITY OF TWENTE.

Faculty of Science and Technology

Volatile Fatty Acid Adsorption and Hyperthermia Regeneration of Magnetic Nanoparticle Impregnated Resins

Ali Nazari Khoorasgani

M.Sc. Thesis in Chemical Science & Engineering
(Track CPE)
December 2021 - August 2022

Chairman:
prof. dr. ir. B. Schuur
External Supervisor:
prof. dr. ir. R. G. H. Lammertink
Daily Supervisor:
phd. candidate V. Elhami

Sustainable Process Technology Group
Faculty of Science and Technology
University of Twente
P.O. Box 217
7500 AE Enschede
The Netherlands

Abstract

Strategically reducing anthropogenic greenhouse gas emissions involves leveraging circular economies through the utilization of wastestreams and green electrification. This thesis introduces a innovative methodology for valorizing volatile fatty acids, co-produced as by-products of anaerobic digestion in biowaste streams. The proposed approach involves the utilization of an adsorptive composite material with the capability of hyperthermia regeneration, activated by Neels and Brownian relaxation mechanisms. The composite material consists of Amberlite PS/DVB XAD1180N (hydrophobic polystyrene crosslinked with divinylbenzene) resins impregnated with superparamagnetic magnetite nanoparticles (Fe_3O_4 functionalised with oleic acid coating, MNP). The synthesis of MNP, capable of generating heat under alternating magnetic fields (hyperthermia), is achieved through the co-precipitation method. These nanoparticles are subsequently employed for impregnation into the resins by slowly evaporating the swell-inducing solvent toluene. This process occures over a span of five hours at vacuum conditions inside a rotary evaporator, under an oscillating pressure in the range of 230-290 mbar at a fixed temperature of 80°C, or very slowly within a 15-day timeframe under a fumehood at a slight under pressure and 20°C.

The impregnation process, characterized by diffusional and capillary regimes, is elucidated through a developed and validated numerical model involving unsteady-state partial differential equations, providing insights into the diffusion of magnetite nanoparticles into the resin matrix. A comprehensive characterization strategy, encompassing scanning electron microscopy (SEM) and atomic absorption spectroscopy (AAS), coupled with numerical simulations, revealed that the magnetite nanoparticle content of the composite material is 15.2% for the 15-day trial and 5.0% for the 6-hour trial. In the latter case, the diffusivity of magnetite nanoparticles was approximately $2\text{x}10^{-5}\,\frac{\mu m^2}{s}$ during diffusional impregnation.

Moreover, hyperthermic examinations of the composite material indicate that the embedded magnetite nanoparticles within the Amberlite series resins retain their hyperthermic capabilities. A maximum specific absorption rate of 3.5±0.7 kW/kg (rate of energy per kg of magnetite nanoparticles embedded) is achieved when exposed to an alternating magnetic field of 25 mT with a frequency of 52 kHz. Additionally, zero-length column adsorption and batch adsorption experiments, in combination with HPLC and IC analyses, demonstrated that the embedding process results in a reduction of active hydrophobic adsorptive sites and may have introduced steric hindrance in adsorption rates. Specifically, the initial adsorptive capacity of polymeric beads for capturing volatile fatty acids (VFAs) is diminished by a total of 22% when tested on artificially generated representation of fermented biowaste containing VFAs and commonly found salts in wastestreams. Further investigation using SEM revealed that the MNP primarily reside in the outer shell of the beads, introducing mass transfer limitations and active site blockage. SEM images demonstrated the penetration depth of the magnetite nanoparticles was approximately 1.5 μm. Observations revealed that the stability of the magnetite nanoparticle layer on the outer shell was compromised when immersed in sonification baths or when in contact with fluids characterized by a high Reynolds number. Accordingly, this proof of concept signifies viability within laminar flow conditions.

Keywords: Composite material, Diffusional impregnation, Magnetic nanoparticles, Magnetite synthesis, Hyperthermic regeneration, Adsorption, Zero length column, Batch adsorption, Volatile fatty acids, Neels relaxtion, Brownian relaxation, Specific absorption rate, Numerical diffuisonal model, Unsteady state numerical simulation, Nanoparticle penetration depth, Nanoparticle diffusivity

Contents

Abbreviations

EU	European Union
VFA	Volatile Fatty acids
MNP	Magnetic Nanoparticle
PFD	Process Flow Diagram
AMF	Alternating Magnetic Field
SAR	Specific Absorption Rate
PS/DVB	Polystyrene Crosslinked with Divinylbenzene
HAc	Acetic Acid
HPr	Propionic Acid
HBu	Butyric Acid
HLa	Lactic Acid
HPLC	High-Pressure Liquid Chromatography
IC	Ion Chromatography
UV-vis	Ultraviolet and Visible
ZLC	Zero Length Column
PDE	Partial Differential Equation
AAS	Atomic Absorption Spectroscopy
SEM	Scanning Electron Microscopy
NP	Nanoparticles
ANP	Nanoparticles with Attractive Interactions
RNP	Nanoparticles with Repulsive Interactions
RI	Refractive Index
RID	Refractive Index Detector
VID	Variable Wavelength Detector

Chapter 1: Introduction

At the start of this decade, 86 million tonnes of biowaste are produced from municipalities and industries in The European Union (EU) [1]. In waste management industry, some of these biowaste are converted by anaerobic digestion to volatile fatty acids (VFA), biogas and carbon dioxide [2]. The production of these products facilitates a circular economy. VFA can take the role of a platform chemical from which many useful products are manufactured [3], [4]. Furthermore, separation of VFA is a necessary component in biogas upgrading plants. A biomethane product must be purified from VFA and other contaminants before being sent into the gas grid.

In this Master Thesis, adsorption of VFA by magnetic nanoparticle (MNP) impregnated resins are investigated. These resins are intended to be incorporated in the adsorption columns of a wastewater treatment plant. The upstream section of this treatment plant produces a mineral rich stream that also contains VFA [5]. The process flow diagram (PFD) of the hypothetical process plant is shown in Figure 1.1.

By using impregnated adsorptive beads and an external alternating magnetic field (AMF) over the beads, a novel method of heat delivery in adsorption columns during the regeneration/desorption cycle is achieved. Hyperthermia generates heat from the resins inside and achieves a better heat distribution. The desorption stage carbon footprint of the column under this circumstance is enhanced since the direct conversion of electricity to heat is enabled, and the use of pre-heated service flow is no longer necessary. Furthermore, if the adsorption column is operated under vacuum conditions, subsequent condensation of water on the adsorption beads will not occur rapidly.

This approach allows for a carbon-neutral route to desorption via electrification. The electrification of adsorption columns in the industry is an alleviation route for global climate change. This method aids the conversion of green electricity into heat [6].

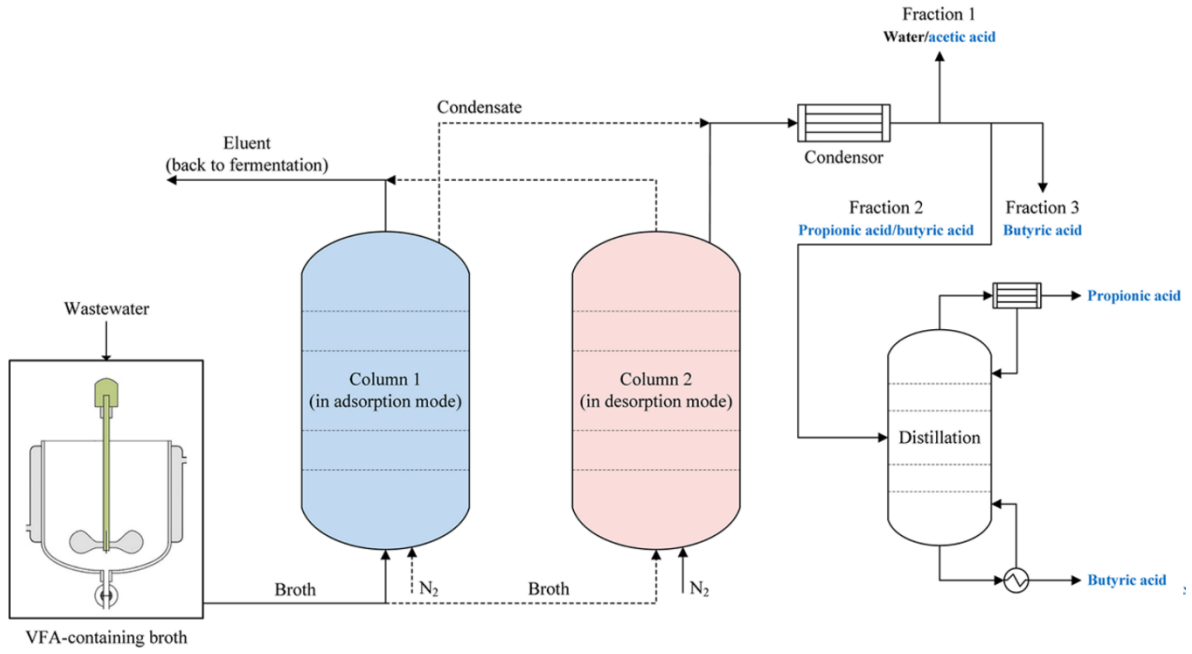

Figure 1.1, Bioprocess plant for treatment of wastewater [5].

Previously, these specialised resins embedded with MNP were made by adding MNP during the suspension polymerisation reaction used to produce crosslinked polystyrene beads [7], [8]. Ph.D.

candidate V. Elhami has synthesised MNP embedded beads via this method. These beads embedded with MNP generate heat under an AMF. Heat diffusion from particle's core allows a better desorption efficiency of VFA by producing water bubbles inside the capillary channels of the porous embedded beads.

In this assignment, the synthesis of similarly magnetically active adsorptive beads is conducted via an impregnation process frequently used in catalyst preparation. Two distinguished regimes of impregnations identified in the catalyst industry are analogous to the impregnation method used in this research. Both methods differ in the amount of solvent utilised in the drying process under vacuum. They are referred to as diffusional (wet) and capillary (dry) impregnation processes [9]. In the former mode, an excessive amount of solvent is used, while in the latter, the amount of solvent is limited and equals the porous volume inside the adsorptive support. In both instances, the adsorptive surface (support) is placed under vacuum conditions to remove entrapped air. The impregnation process in this research utilises an excessive amount of solvent, while the swelling effect of the polymeric resins is exploited. Moreover, the impregnation process is conducted via normal and intensified conditions. In the latter, high temperature and vacuum conditions are imposed on the system, while the former impregnation proceeds at laboratory temperature and atmospheric pressure.

Furthermore, a numerical approach in tandem with the lab-scale impregnation process is implemented to evaluate the MNP profiles obtained by analytical methods. By using this numerical method, the diffusivity coefficient of MNP into crosslinked beads during the impregnation process is calculated. Additionally, the adsorptive and hyperthermia performance of synthesised impregnated beads are analysed with artificially made fermented wastewater and AMF.

Chapter 2: Theory of resin impregnation with magnetic nanoparticle

In an impregnation process [10]–[17], a functionalised diffusive compound undergoes diffusive mass transfer from a liquid solvent towards a solid support (adsorptive medium) at which it becomes immobilised or trapped. By scrutinising this phenomenon, four core elements are defined for impregnating resins capable of adsorption of VFA and activating hyperthermia inside them. These elements are the following:

- A diffusive compound enabling heat generation under AMF.
- A suitable surfactant for the diffusive compound.
- A solvent to act as a medium of mass transfer for the diffusive compound.
- An adsorptive support such as a porous resin.

It has previously been shown that magnetite nanoparticles suspended in a solvent [18], [19] or entrapped in a medium [20] can produce heat under an AMF. This type of liquid is referred to as a ferrofluid that shows superparamagnetic behaviour and attracts static magnetic fields. To introduce hyperthermia capabilities to an adsorptive resin, a ferrofluid is synthesised. This fluid is a combination of coated MNP suspended stably in a solvent and is utilised in an impregnation process to facilitate the transfer of MNP from the liquid phase to the solid adsorptive phase.

2.1 Magnetic nanoparticle

Iron oxide-based magnetic nanoparticles such as magnetite have gained immense application in nanotechnology due to their availability, superparamagnetic properties, and high magnetic saturation field [21]. One commonly used type is magnetite and this MNP is significantly sensitive to magnetization under an AMF.

Magnetite crystalline structure is characterised by an inverse spinel structure [21]. In this cubic lattice structure, ferric cations (Fe^{3+}) occupy all the tetrahedral sites in addition to half of the octahedral sites, while the ferrous cations (Fe^{2+}) preferentially occupy half the octahedral sites. This site allocation happens due to minimising the crystal field stabilisation energy. In this compound, superparamagnetic properties appear when the structures' dimensions are reduced to a single-domain region around 20 nm [21].

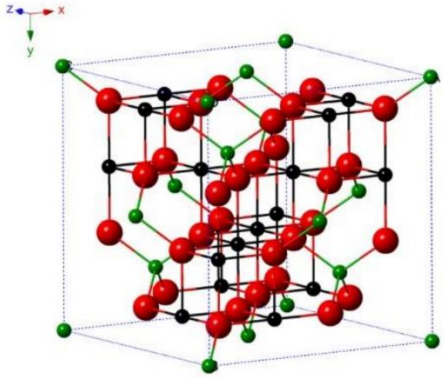

Figure 2.1, Crystal structure of magnetite (Fe_3O_4). The green, red, and black balls each represent ferric ions, oxygen ions and ferrous ions chronologically [22].

In the magnetite crystal structure, ferric cations at tetrahedral and octahedral sites have opposite spin moments because they are coupled identically in an inverse spinal crystal. As a result, ferric cations' net magnetic moment results in complete annihilation [23]. In contrast, the ferrous cation magnetic moment is aligned with the rest of the octahedral sites. The ferromagnetic behaviour of magnetite is attributed to the aligned magnetic domains of the ferrous ions clouded by oxygen electrons shell inside the crystal lattice.

As the magnetite dimensions are reduced from bulk compound to nanoscale particles, the ratio of surface ferrous cations with a lower coordination number is increased while the concentration of oxygen atom is reduced. Thus, the valence electrons are curtailed [24]. Consequently, the ferrous cations' influence on induced magnetism is amplified.

Any ferromagnetic compound influenced by AMF demonstrates retentivity and coercivity. A reduction in the dimensions of magnetite to the nanoscale will cause the number of exchange-coupled spins, which spontaneously and disproportionately negates magnetic reorientation, to deplete [23]. Therefore, superparamagnetic characteristics are revealed as the opposition to magnetic fluctuation becomes much less [25]. Although reducing the size of the MNP to below 10 nm will reduce the magnetic saturation level as the magnetic nanoparticles start to behave more like an individual atom rather than an ensemble of bonded atoms with superparamagnetic characteristics.

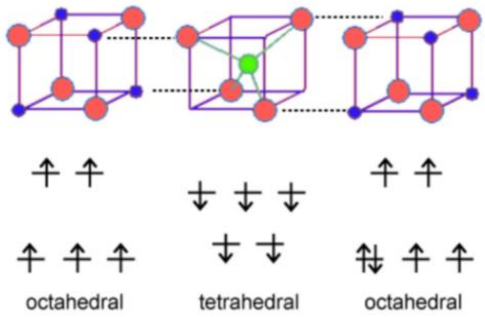

Figure 2.2, Electron configuration of atomic orbitals of iron cations at interstitial sites of magnetite (*https://chem.libretexts.org*).

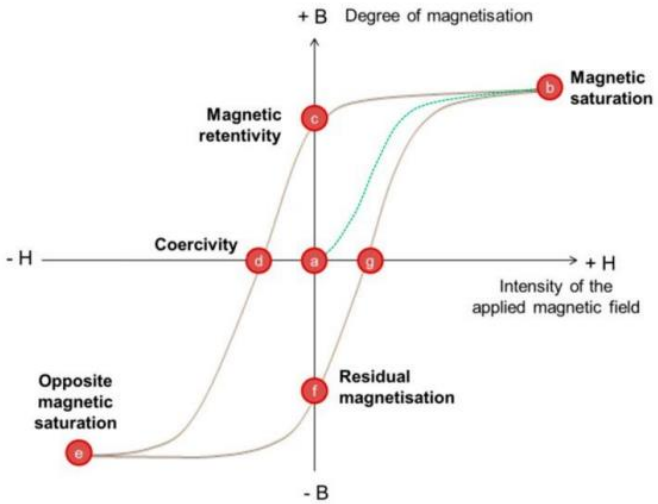

Figure 2.3, Superparamagnetic behaviour (a) occurs at the nanoscale where magnetic coercivity and retentivity are diminished [23].

2.1.1 Synthesis of MNP via co-precipitation

There are multiple production alternatives for the synthesis of magnetite. These approaches include co-precipitation, hydrothermal, pyrolysis, sol-gel, microemulsion, sonochemical, electrodeposition, and polyol [26]. In these approaches, producing viable superparamagnetic MNP depends on controlling the size distribution of the crystalising nanoparticles. As a production condition, the crystalline dimension of the particle should be above 10 nm to ensure magnetite MNPs demonstrate relatively appreciable superparamagnetic properties. On the other hand, their size should be smaller than the pore diameter of adsorptive resins. The latter condition is essential during the impregnation of the resins.

Of all synthesis methods, co-precipitation is the one commonly applied in the industry since it has a straightforward scalable process that consumes less energy and is time efficient. In this method, magnetite is produced from a mixture of iron (III) chloride anhydrous and iron (II) chloride tetrahydrate initially mixed in an acidic mixture. Crystallisation is induced by changing the initial acidic aqueous medium into an alkaline environment. A surfactant is also added to the solution after the product material has yielded by crystallisation. During the crystallisation, a constant stream of nitrogen flow is introduced to the aqueous medium to limit the oxidation of magnetite into other phases and prevent the formation of impurities. The chemical reaction Equation (2-1) describes the overall reaction mechanism.

$$Fe^{2+} + 2\,Fe^{3+} + 8\,OH^{-} \rightarrow Fe_3O_4 + 4\,H_2O \qquad (2\text{-}1)$$

The size, morphology, and superparamagnetic behaviour of synthesised magnetite via co-precipitation depend on the operational variables. Significant synthesis variables are the following:

- Initial pH of mother liqueur
- Molar ratio of $FeCl_3 : FeCl_2.4H_2O$
- Final pH after digestion
- Temperature
- Rate of stirring
- Duration of crystallisation

A key side reaction affecting the impurity formation during crystallisation is the oxidation of ferrous ions to ferric ions. Furthermore, this clarifies the need for a constant nitrogen stream during the crystallisation process, which depletes oxygen from the reaction tank. Furthermore, to facilitate rapid nucleation and limit the MNP growth, it is recommended to increase the contact surface between the two liquid phases during the addition of the precipitating agent.

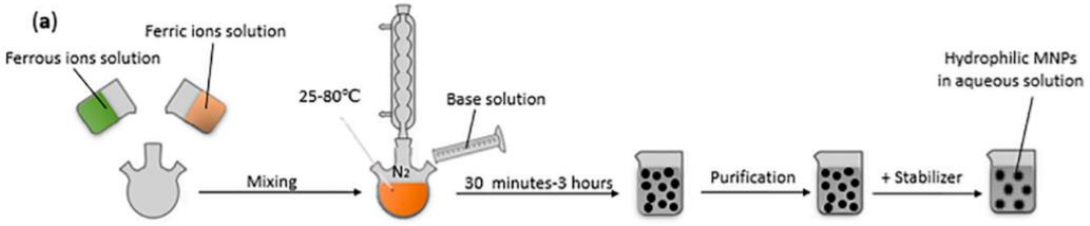

Figure 2.4, coprecipitation synthesis of magnetic nanoparticles [22].

In a study, surfactants with a volumetric ratio of 0.5% - 1% compared to the mother liquor were used. Additionally, ammonium hydroxide was used as precipitating agent [27]. In another study where the initial and final pH of the mother liquor during the starting nucleation phase and the final part of the growth phase were examined, it was demonstrated that a starting pH of 2 with an after-digestion pH of 10 is capable of producing magnetite with the quality sought in this research [28]. Similar comparative optimum results were obtained in another study at which a final pH of 10 and an operating temperature of 45°C were included in their results [29]. Their study also included a sensitivity analysis on the speed rate of mixing. It was revealed that crystalline particles produced at a stirring rate of 400 rpm had a better superparamagnetic characteristic. By looking at synthesis cases and optimising the parameters, the conditions given in Table 2.1 is suggested for the synthesis of MNP. The complete synthesis procedure is provided in Appendix A.

Table 2.1, Proposed parameters for coprecipitation of coated magnetite.

Parameter	Value
Initial pH using HCL	2
Molar ratio of ferric salt to ferrous ion	2
Final pH after digestion	10 - 12
Temperature	20 - 80°C
Rate of stirring	400 rpm
Surfactant volumetric ratio	0.85%
Precipitation initiator	ammonium hydroxide

2.1.2 Hyperthermia of MNP

The collapse of the magnetic hysteresis loop under a magnetic field indicated by dashed line in Figure 2.3, occurs due to the superparamagnetic behaviour of MNP. Consequently, since magnetic coercivity and retentivity does not exist in such material, the oscillation of the induced magnetism to maximum opposites under an AMF allows the generation of heat. This method of heat generation is hyperthermia.

When an AMF influences MNP, their magnetic moment undergoes oscillation, and thus, heat is generated through Neel and Brownian relaxation mechanisms [20]. These mechanisms are dependent on the dynamic behaviour of a single subdomain particle in an AMF [18], and both are characterised by relaxation time [30]. Neels mechanism is the result of the rotation of the magnetic moment within the crystalline structure, while the Brownian mechanism is the rotation of the particle as a whole which contributes to heat generation via mechanical and frictional forces [18].

The thermal heat production capability of MNPs under an alternating magnetic field to act as an energy production source is quantified using a specific absorption rate (SAR, Q_{SAR}). Experimentally, this parameter is obtained by using its mathematical definition is given in Equation (2-2) [18].

$$Q_{SAR} = c_p \frac{dT}{dt} \tag{2-2}$$

The physical properties of the medium containing the superparamagnetic compounds enabling hyperthermia under an AMF contributes to the overall SAR of the material. Physical properties that are contributing to the magnitude of experimentally observed SAR are suspensibility, concentration, size, and morphology of MNP, viscosity, density, magnetic permeability, and specific heat of the medium [19], [31]. These parameters affect the heat transfer mechanism and its macroscopic heat transfer regime.

Besides the properties of the MNP and the mixture medium containing it that have a direct effect on hyperthermia, heat generation via this method can also be increased by changing the amplitude or the frequency of the AMF [18], [28]. Magnetite nanoparticles reach their saturated magnetisation when the amplitude of AMF is higher than 300 mT [28]. It is expected that increasing the amplitude of the AMF until this level will enhance the magnitude of hyperthermia.

Additionally, hyperthermia studies on multidomain ferrite and subdomain ferrite, which are materials similar to MNP and are capable of hyperthermia, has been shown that increasing the frequency of AMF into orders of MHz from kHz can increase hyperthermia significantly [18].

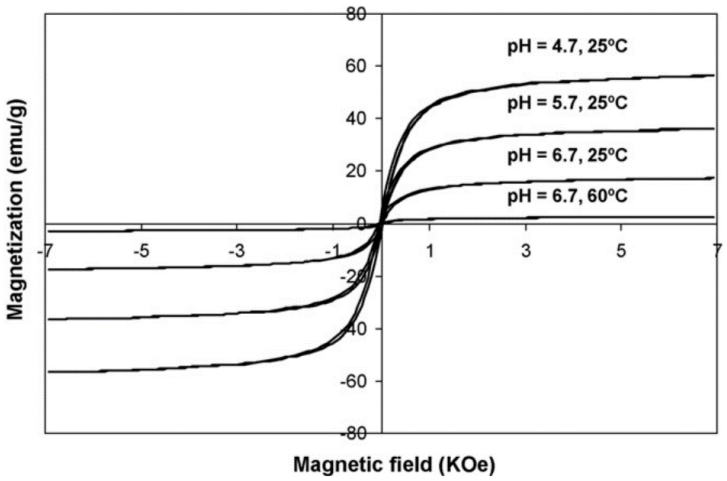

Figure 2.5, Superparamagnetic MNP synthesised at various initial acidic solution reach their saturated magnetisation at approximately 300 mT [28].

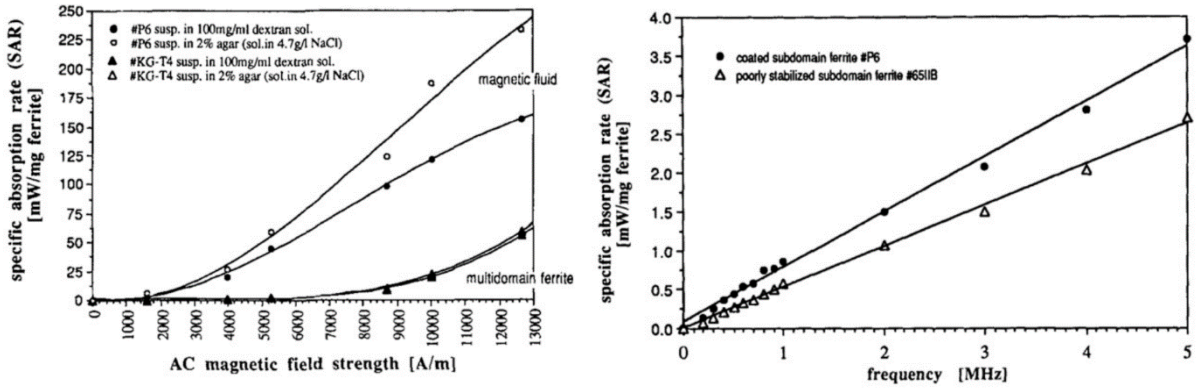

Figure 2.6, hyperthermia enhancement by increasing frequency and amplitude [18].

2.2 Surfactant

MNP are susceptible to oxidation and agglomeration. If these reactions are not considered, superparamagnetic properties will diminish over time after the synthesis [32]. At a temperature range of 110-230 °C, magnetite oxidizes to maghemite and, if the temperature is further elevated to above 250°C into hematite [27]. A change in the oxidation phase modifies the magnetic saturation field levels of the MNP. Consequently, hyperthermia heat production inside impregnated resins becomes less effective [28]. Thus, to enhance and sustain the capability of magnetic nanoparticles, it is essential to use a surfactant.

Furthermore, this surfactant satisfies other objectives besides preserving the MNP from deterioration during the impregnation process. The coating can be tuned to provide the MNP with a hydrophobic layer. This layer attracts hydrophobic mediums such as polystyrene crosslinked with divinylbenzene (PS/DVB) resins. The affinity generated through the attraction of the hydrophobic coating and the porous support allows the adsorption and diffusion of the MNPs into porous support. For this reason, hydrophobic organic surfactants are suitable to utilise when considering the impregnation of hydrophobic mediums. By examining previous works, these types of surfactants are mostly carboxylic acids. In most cases, the surfactants bond with the MNP through an esterification reaction [27]. The carboxyl group of the acidic surfactant molecule surrounds the hydroxyl groups of ferrihydrites inside the magnetite. It is also expected that hydrogen bonding between the surfactant and the MNP is also an essential factor in the stability of the surfactant. In literature and bioindustries, oleic acid has been commonly used for such purposes [32], [33].

The coated MNP should have appreciable suspensibility inside the solvent of choice during the impregnation of coated MNP into the medium. An organic solvent can suspend MNP coated with a hydrophobic layer. The compatibility of the solvent and the coating is of crucial importance. Moreover, the suspended coated MNP should not become too large due to the addition of the extra coating. If the former is the case, size exclusion enforced by the pore size of the resins hinders impregnation of the medium by large coated MNP. Thus, besides providing the affinity for diffusion, the size of the coating influences the extent of diffusion. Regarding hyperthermia, larger coated MNP have a lower magnetic saturation field. The additive layer forms non-magnetic domains that reduce intraparticle magnetic interactions [27]. Finding a suitable surfactant that only creates a thin coating layer is of great interest. Other found alternatives to an oleic acid coating that allows for a small layer are hexanoic and heptanoic acids. In a study [27], a comparison of oleic acid and a hexanoic acid surfactant revealed that the type of surfactant has a great significance on electrical conductivity and magnetic properties.

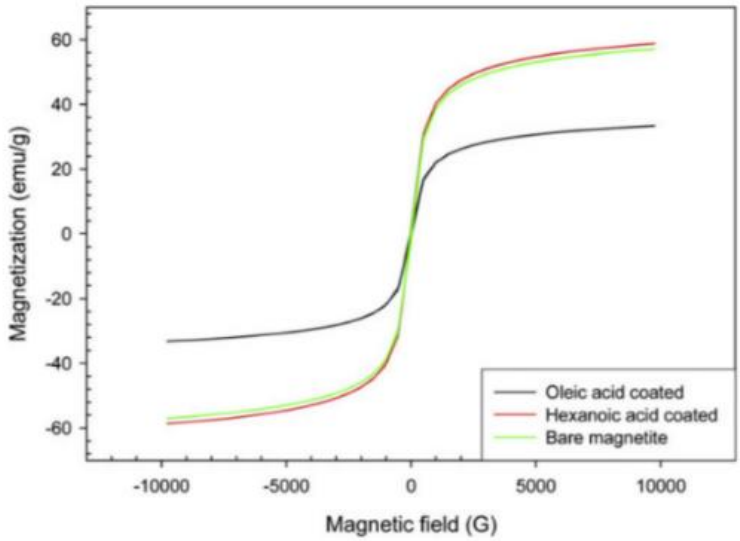

Figure 2.7, Magnetic properties of magnetite nanoparticle synthesized at 90 °C with 0.8% (v/v) coating agent [27].

It has been deciphered that better superparamagnetic capabilities and smaller size coated MNP is obtained when hexanoic acid is utilised as a surfactant instead of oleic acid [27]. Thus, this coating provides some advantages.

Oleic acid has found tremendous application as a surfactant of magnetite in the biomedical field because this biocompatible coating induces hydrogen bonding inside the aqueous solution, which allows the

suspension of MNP [33]. Furthermore, due to its long hydrocarbon chain structure, it also demonstrates excellent suspension inside organic solvents. In our instance, suspension and retainment of magnetic nanoparticles in water are not sought after, but its suspension in an organic solvent during the impregnation phase is crucial. On the other hand, due to the large molecular size of oleic acid molecules, hydrophobic interactions between oleic acid and the hydrophobic resins are more pronounced. Therefore, both hexanoic acid and oleic acid show merit to be suitable surfactants for MNP in this study.

Table 2.2, Comparison of using oleic acid or hexanoic acid for MNP coating.

Oleic acid		Hexanoic acid	
Advantages	Disadvantages	Advantages	Disadvantages
More hydrophobic	Bigger MNP particles	Smaller MNP particles	Less hydrophobic
Better stability		Better Superparamagnetic characteristics	Toxicity
Stable suspension in organic solvents			
Biocompatible			

2.3 Solvent

A solvent is required to introduce coated MNP into the resins during the impregnation. This solvent is utilised to act as a medium for the diffusive mass transfer of MNP into the porous medium. If the coated MNP are not sterically hindered due to their size, driven by their affinity gained by their coating, diffusion toward the core of the adsorptive medium continues during impregnation. The solvent must be capable of suspending the coated MNP. Otherwise, they will accumulate at the bottom of the flask and not contribute to the impregnation process.

In literature, impregnation methods are applied to facilitate the diffusion of material into resins [11]–[17]. In some of these approaches, the resins are swollen by the solvent containing MNP. The expansion of the polymeric network is crucial, as it influences the size exclusion effect of the medium on the diffusive material. Thus, a solvent capable of swelling the resin is beneficiary in two ways. Initially, it allows a higher inclusion by increasing the pore size. Subsequently, after the solvent removal at the end of the impregnation process, it traps the diffused materials by deswelling the resins.

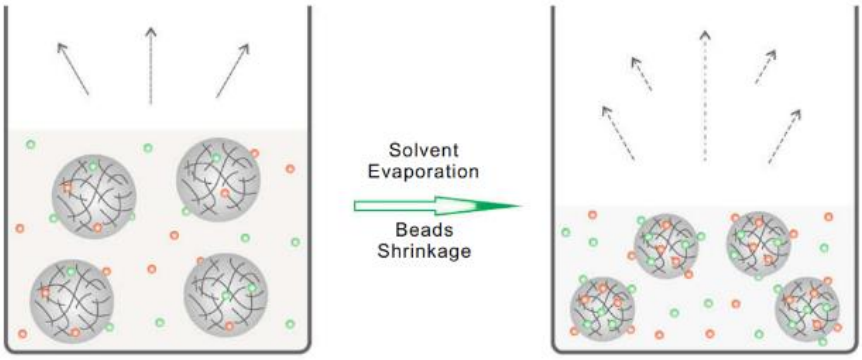

Figure 2.8, Solvent swelling facilitates impregnation [11].

The solvent of choice should induce reversible swelling in the resins by an adequate degree. This phenomenon will allow a better distribution of MNP into the resin's matrix [34]. On the other hand, it should not dissolve the polymeric resins or deteriorate the crosslinks within its matrix. The solvent must

be hydrophobic to allow penetration into the resin. Moreover, the solvent should not have a strong affinity for the coated MNP to improve the exchange of medium for the coated MNP [17].

During the impregnation process, the solvent is slowly evaporated under vacuum conditions. These conditions are essential to reduce back-diffusion of the MNP and to liberate additional adsorptive sites while reducing capillary forces. Evaporation under vacuum conditions at a higher temperature point will increase the Brownian motion of the MNP and reduce viscosity; hence diffusivity is improved.

By evaluating previous impregnation methods implemented [12], [16], [14], [13] , the most commonly used hydrophobic solvents that meet all the criteria as mentioned earlier are toluene and n-hexane. Toluene, compared to n-hexane, has a higher boiling temperature and, due to the aromatic ring included in its molecular structure, allows a better electron transference. N-hexane is volatile, and its swelling effect is also significant. Both n-hexane and toluene are suitable candidates for the impregnation of hydrophobic resins. However, since toluene has a higher boiling point, its chosen as the optimum solvent for impregnation.

It was considered that the addition of cyclohexane to toluene should reduce the swelling effect of the solvent mixture. At first glance, this combination of solvents seemed promising to tune the swelling effect, but it became apparent during the impregnation process that this mixture evaporates erratically and increases the back-diffusion of the MNP. Consequently, this option is infeasible. Nevertheless, a combination of two organic solvents which produce an azeotrope may be evaporated at a constant rate and in a predictable manner with tunable swelling properties. Thus, they may be applied to the impregnation process. Nevertheless, pure toluene had manageable swelling effects on hydrophobic resins.

Table 2.3, Advantages, and disadvantages of candidate solvents for impregnation.

Solvents	toluene	n-hexane	cyclohexane	toluene and cyclohexane
Advantages	High swelling Higher boiling temperature	High swelling	Mediocre boiling temperature	Controlled swelling
Disadvantages		low boiling temperature	low swelling	low swelling irregular evaporation

2.4 Resin

The resin functions as an adsorptive support both for the coated MNP and the VFA. Adsorption and diffusion of both compounds are necessary for the applicability of the impregnated resins. Different affinities may be utilised for the adsorption of both compounds. All VFAs have a carboxylate group inside their molecular structure. Dependent on the pH of the aqueous stream, these compounds are in equilibrium with their negatively charged conjugate form. Therefore, it is possible to use ion-exchange resins for the adsorption of VFAs [35], [36]. Resins functionalised with amines are one common type of these resins.

The following reaction kinetics described in Equation (2-3) and (2-4) applies to a resin that is functionalised with amines. If the resin matrix includes ammine compounds, ion-exchange reactions are applicable for the adsorption of our target acid [36]. If quaternary amines are already incorporated inside the resin, Equation (2-3) does not apply as it is already positively charged. Quaternary amines

can directly capture the acids in their carboxylate form, and other amines can only attract the acids through hydrogen bonding or proton transfer [5].

$$R_XNH_{3-X} + H_2O \leftrightarrow R_XNH_{4-X}^{+} + OH^{-1} \quad (2\text{-}3)$$

$$R_XNH_{4-X}^{+} + A^{-} \leftrightarrow R_XNH_{4-X}A \quad (2\text{-}4)$$

Although this approach seems satisfactory, competitive adsorption of mineral acids in the fermented wastewater makes adsorption through this affinity an unattractive approach [5]. Thus, this type of affinity does not facilitate the selective adsorption of VFA from fermented wastewater.

VFA have an apolar aliphatic organic structure. Therefore, it is also feasible to adsorb VFA into resins with a hydrophobic resin that amplifies Van der Waals interactions. There is a proportional relation between the length of an aliphatic chain of a VFA and its initial adsorption rate with a hydrophobic resin [37]. Using hydrophobic interactions as the main driving force for adsorption streamlines the downstream process as this type of affinity is pH-independent. Bicarbonate and carbonates concentration in equilibrium with gaseous carbon dioxide act as buffer systems and limit the pH window of the feed stream of the process [36]. Biowaste streams and their fermented effluent are complex mediums with fluctuating pH levels, and the stream's pH may deviate from the operational pH window for the selected resin. Thus, incorporating resins adsorbing via hydrophobic interactions is a better alternative than resins adsorbing via electrostatic interactions. Furthermore, this affinity has negligible competitive adsorption from other compounds commonplace in fermented wastewater streams.

Table 2.4, A general comparison of various resins and their adsorptive interactions.

Commercial name	Matrix	functional group	Interaction	Reference
Ambelyst A21	polystyrene cross-linked with divinylbenzene	tertiary amine	hydrophobic and electrostatic	[36]
MCM-41	mesoporous silica nanoparticle	tertiary amine	electrostatic	[35]
Purolite A133S	polystyrene cross-linked with divinylbenzene	tertiary amine	hydrophobic and electrostatic	[37]
Activated carbon	none	none	hydrophobic	[37]
Amberlite XAD4	polystyrene cross-linked with divinylbenzene	tri-*N*-butyl phosphate	hydrophobic	[10]

Besides providing the affinity for impregnation and adsorption, the resins should be highly porous and have a high surface area per gram of resin, and this will provide enough adsorption sites for VFA adsorption and impregnation with the MNP.

Hydrophobic porous mediums such as PS/DVB resins are commercially available for the adsorption of fermented products in the bioprocess and pharmaceutical industries. PS/DVB resins have a highly aromatic structure and are functionalised with various solvents [5], [37]. Metalation reactions occur effectively in some of the aromatic rings of such resins [34]. In some instances, the final resins are functionalised using intermediary bromination and lithiation reactions. Commercial PS/DVB resins like the ones in the Amberlite series have gained traction for multiple impregnations and functionalisation applications [38].

Many different configurations were found from commercial vendors of PS/DVB resins. Since it is of interest to impregnate a resin with MNP that is influenced by an AMF, it is pragmatic to choose a less polar resin with a large pore diameter and a relatively high surface area for adsorption.

A polar resin will dampen the vibration frequency of the MNPs and reduce the amount of heat generated per site during hyperthermia regeneration. As another critical feature, the resins' pore diameter significantly affects the diffusion rate of MNP during impregnation. A reduction in the pore diameter size will cause steric obstruction of MNP diffusion during impregnation.

Furthermore, it is beneficial that the resins demonstrate a high degree of reversible swelling when brought in contact with a preferred organic solvent during the impregnation step. The swelling phenomena will allow an even distribution of the diffusing particle during the impregnation process [34].

Table 2.5, a comparison of commercial polystyrene crosslinked with divinylbenzene resins

Commercial name and supplier	Radius (μm)	Surface area ($\frac{m^2}{g}$)	Pore size diameter (nm)	Commercial application
AmberLite, XAD1180N (Dupont)	475 nm	500	40	Immobilisation of enzymes separation of fermentation products
AmberLite, XAD1180N (Supleco)	350-600	450	30-40	Separation of hydrophobic compounds
AmberLite, XAD16N(DuPont)	450	800	15	Removal of non-polar compounds from polar solvents

PS/DVB XAD 16N provides a higher surface area than other commercial types but has a much narrower pore diameter that will enforce a stricter steric diffusion of MNPs during impregnation. In contrast, PS/DVB XAD1180N model has a large pore diameter, and thus diffusion will continue more efficiently during the impregnation process. Furthermore, like the other type, it swells similarly to organic solvents, selectively adsorbs VFA by hydrophobic interactions, and is non-polar. The impregnation of this type of resin is further investigated in this research.

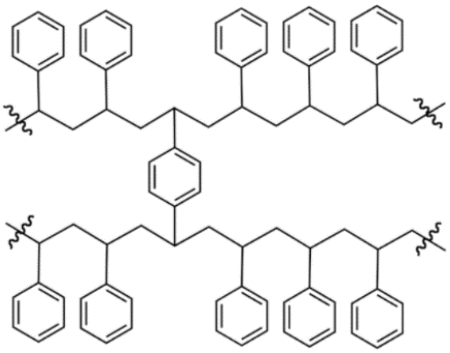

Figure 2.9, Molecular structure of PS/DVB.

2.5 Decision summary

The decisions about the four main components in the impregnation process as discussed is repeated here in this section. These set of choices are interconnected and a decision regarding one component has inevitable influence over multiple components. In deciding the combination of parameters, their interconnection and influences were examined thoroughly.

Table 2.6, decision summary regarding components in the impregnation process.

Component	Decision
Solvent	toluene
MNP	magnetite synthesised via co-precipitation
Surfactant	oleic acid
Resin	PS/DVB XAD1180N

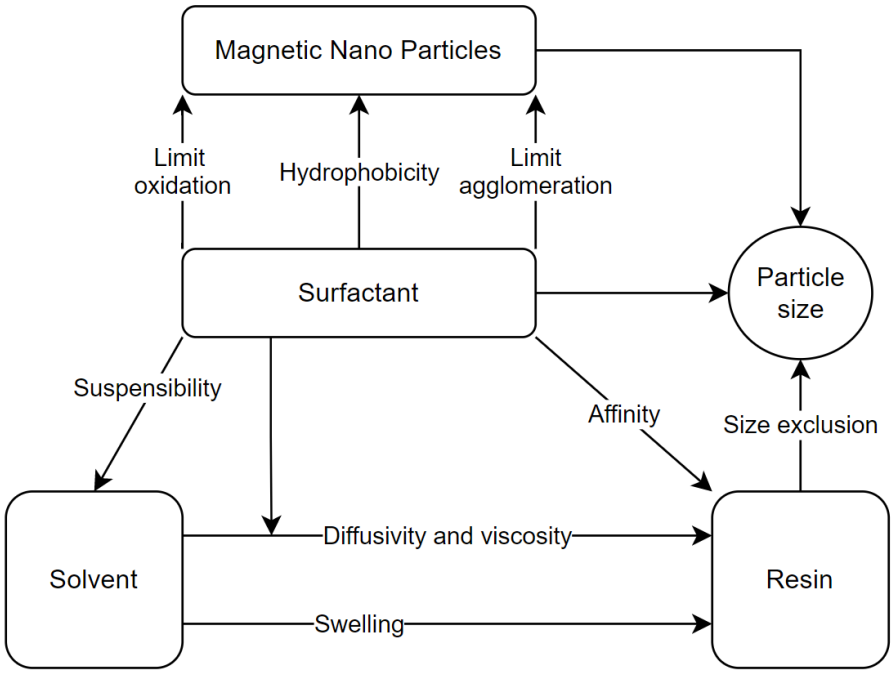

Figure 2.10, The causal interactions between components influencing the impregnation process.

Chapter 3: Materials & methods

The impregnation process at the lab scale is implemented at a rotary evaporator operating at vacuum conditions at 80°C. Similarly, the impregnation is also conducted under a fume hood at normal conditions and compared with the previous method. The required MNP for the impregnation process is synthesised via co-precipitation. Moreover, this process is numerically simulated by applying a discretised method. The distribution of MNP inside the impregnated resins is analysed by analytical methods such as Scanning electron microscopy (SEM) and atomic absorption spectroscopy (AAS). Furthermore, an agreement between the analytical method and the numerical analysis is established. Finally, the adsorptive performance and hyperthermia regeneration of the resins are evaluated.

3.1 Chemicals

For the synthesis of a ferrofluid containing suspended coated MNP, iron (III) chloride anhydrous, iron (II) chloride tetrahydrate, hydrogen chloride (>37%), ammonium hydroxide (>30%), oleic acid (>99%), and toluene (>99%) were purchased from Sigma-Aldrich. The chosen adsorptive medium for impregnation, which is Amberlite® XAD1180N, was also purchased from Sigma-Aldrich. Acetic acid (HAc, >99.7%), propionic acid (HPr, >99.5%), butyric acid (HBu, >99%), potassium chloride (>99%), anhydrous sodium phosphate dibasic (>99%), and anhydrous sodium sulfate (>99%) were purchased from Sigma-Aldrich for the synthesis of an artificially made fermented waste. In this mixture, anhydrous crystalline lactic acid (HLa, >98%) was kindly provided and synthesised by Ph.D. candidate M. Gholami. Additionally, nitric acid was obtained from Sigma-Aldrich for atomic absorption spectroscopy of impregnated resins.

3.2 Experimental methods

Two alternative approaches to the suspension polymerisation route for MNP embedding to PS/DVB resins are considered. In the primary approach, impregnation is pursued in a rotary evaporator operating under vacuum conditions at 80°C. In the secondary approach, the solvent is evaporated at room temperature and atmospheric pressure in a prolonged process. Subsequently, the hyperthermia capability and adsorptive performance of the impregnated resins are evaluated in batch, zero-length adsorption and hyperthermia experiments.

3.2.1 Impregnation at intensified conditions

The impregnation of the resins proceeds efficiently under two essential process conditions. First, vacuum conditions must be applied to the system. Second, the process parameters should be adjusted such that the solvent evaporates slowly at high temperatures under vacuum conditions. Nevertheless, the evaporation rate should not be too slow as it will render the process costly by increasing the operational costs.

The rationale for impregnation under vacuum is to enhance the release of adsorbed air from the pore channels and make the adsorptive sites more accessible, and this allows setting the pre-occupied adsorptive sites free.

During the impregnation, the solvent containing the suspended coated MNP (ferrofluid) impinges through the channels and causes swelling. The coated MNP diffuses further into the core of the beads via the solvent medium inside the resins as impregnation continues. Eventually, the solvent must be

evaporated to reach a final product in which the solvent is completely withdrawn from the beads. The removal of solvent causes the deswelling and the entrapment of the MNP.

The forward diffusion of MNP directed toward the core of the beads occurs due to the affinity of the oleic acid functionalisation of the MNP thermodynamically favouring hydrophobicity. Another factor influencing the diffusivity of MNP is the rate of evaporation. If solvent removal from the pore channels is too rapid, it will drag the suspended MNP toward the beads' external surface. The solvent evaporation rate must be optimised to alleviate back diffusion. This effect is a multi-component mass transfer phenomenon. A feasible solvent evaporation rate that is harmonious with the impregnation duration must be determined.

In contrast, the evaporation rate should not be too slow since an ample operation time will make the impregnation process inefficient and time-consuming.

Key synthesis variables are investigated by searching relevant literature and finding similar resin impregnation methods implemented before. These variables provide a qualitative range for input variables of a numerical simulation of the impregnation process.

Table 3.1, precedent cases of hydrophobic resin impregnation.

Impregnation case	Mass of diffusive compound	Mass of resin	Volume of solvent	Duration and conditions	Mass ratio
fluorescent dyes diffusion into cross-linked PS beads via chloroform and isopropanol [11].	2-20 mg	100 mg	25 ml	12 hr drying 30 $°C$ 100 mbar	5-50
Cyanex 923 diffusion into MPP via n-hexane[12].	-	-	-	drying at 60 $°C$ 100 mbar	-
TOA-impregnated Amberlite XAD via n-hexane [13].	0.1-0.5 gr	1-5 gr	3 mL	12 hr drying 60 $°C$ 100 mbar	10
Aliquat 336 diffusion into in Amberlite XAD-4 resin via n-hexane [14].	20 gr	20 gr	75 mL	24 hr of mixing and 24 h drying at 40 $°C$	1

In this impregnation process, besides the diffusivity of MNP inside the crosslinked polymeric network of PS/DVB, four input parameters influence the concentration profile and extend of MNP diffusion into PS/DVB. These parameters are the following:

- Mass of MNP suspended in the solvent.
- Mass of resin.
- Volume of the solvent.
- Duration of impregnation.

Inspired by the precedent cases of impregnation and their operational conditions, these parameters are chosen to reflect the operating conditions of the available rotary evaporator feasible for a lab-scale impregnation.

Table 3.2, Process parameters for the impregnation.

Mass of MNP	Mass of PS/DVB	Volume of the toluene	Duration of impregnation	Temperature
0.5 gr	2.5 gr	25 ml	5 hrs	80°C

a) Evaporation rate control in the rotary evaporator

Toluene causes a satisfactory swelling in PS/DVB and has a high vacuum boiling temperature. Its evaporation rate is controlled via a pressure scheme. This is done to ensure that toluene evaporates at a constant rate over time to reduce the back-diffusion of MNP towards the external surface of the beads. A sensitivity analysis of the control parameters is conducted to evaluate the changes in the rate of toluene evaporation inside the rotary evaporator.

The vapour generated inside the rotary evaporator is channelled to a condenser, where it is separated into liquid form. The condenser and the evaporator flask are all interconnected by tubes, and their pressure is regulated by a vacuum pump that is attached to the top of the condenser. Changes in pressure due to evaporation occurs inside the flask, and its effects trickle toward the condenser and finally to the vacuum pump. Thus, differential changes in the flask are not directly monitored. However, regulating the general pressure inside the whole equipment is monitored.

The vacuum pressure within the instrument is regulated by a simple on/off mechanism to control the evaporation rate inside the rotary evaporator. The vacuum pump acts as the final element in this control scheme. The attached mixture flask is immersed inside a hot bath at 80°C. The vacuum pump operates once an upper-pressure threshold is reached.

By observing exponential increases in droplet formation in the condenser when lower sub-atmospheric pressure is reached, a control scheme is inspired.

The evaporation rate increases exponentially when the operating pressure deviates from the saturated pressure of the solvent at the operating temperature. The evaporation rate becomes sensible when the deviation from the saturated pressure of the solvent becomes large. In our case, toluene evaporates at a sensible rate with rapid bubble formation when pressure is reduced to below 245 mbar.

By operating the rotary evaporator without the control scheme, this observation indicates that the driving force for evaporation behaves like an exponentially decaying function as pressure builds up again due to the evaporation of the solvent. Moreover, this evaporating system is susceptible to changes in operating pressure. According to the sensitivity in Appendix B, A 60 mbar change to the operating pressure changes the evaporation rate by factor of 10. It is possible to make the system less sensitive to pressure by reducing the operational temperature, but this adjustment will reduce the diffusivity of MNP and increase the solvent's viscosity.

A combination of rapid and slow evaporation regimes inside the rotary evaporator is incorporated as a suitable approach for impregnation at high temperatures with a controlled evaporation rate. By this methodology, a steady rate of evaporation is obtained.

The vacuum pump's on/off control scheme is exploited to make this system more predictable and obtain a steady rate of evaporation over the impregnation process. In this control scheme, initial rapid evaporation of the system is initiated by reducing the pressure to a low vacuum condition; consequently, pressure builds up rapidly due to the sudden increase in the evaporation rate. By strategically setting the pressure threshold at a much higher value than values regularly used in the rotary evaporator, the rapid evaporation regime goes through a transition, after which the driving force and the evaporation rate reduce simultaneously. These sequenced intervals of rapid evaporation and relaxation allow for slowly evaporating the solvent and thus reducing the back diffusion effect on the MNP.

By doing sensitivity analysis on rotary evaporator control parameters such as the pressure set point and pressure threshold, a feasible pressure profile is obtained for the impregnation process. This scheme keeps the operating pressure below the maximum pressure threshold. Whenever the pressure threshold is reached, a vacuum pump reduces the pressure to the set-point pressure. This pressure shift allows for a comparatively sudden rapid evaporation of the solvent followed by a relaxation period. It is hypothesised that the sudden evaporation affects the liquid phase outside the boundaries of beads more disproportionately than the liquid encroaching inside the pore channels of the porous adsorptive beads. Thus, minimising back diffusion phenomenon inside the beads more efficiently.

The sensitivity analysis with all the trial experiments is provided in Appendix B. The decided profile is qualitatively shown in Figure 3.1 and given in Table 3.3.

Table 3.3, Feasible operating point for impregnation of PS/DVB.

Temperature (T)	Pressure set point (P)	Allowable excessive pressure (dP)	Pressure threshold
80 °C	230 mbar	60 mbar	290 mbar

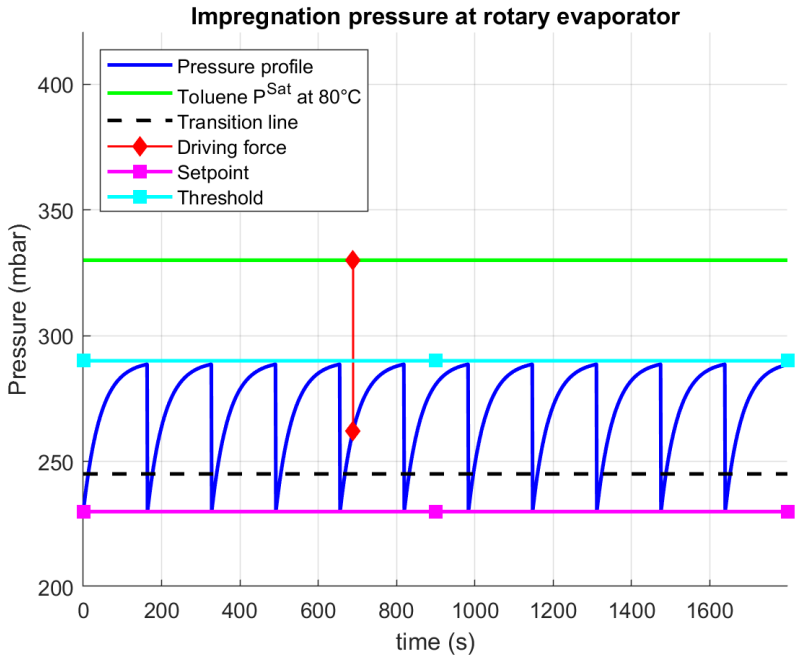

Figure 3.1, A qualitative pressure profile for slowly evaporating toluene during impregnation.

b) Impregnation procedure in the rotary evaporator

In the first step of the process, non-functionalised crosslinked PS/DVB polymeric resins under the commercial name of Amberlite® XAD1180N are pre-treated with water in an adsorption column. This step is crucial to remove any conservative salt or particulates that may have been introduced during the packaging of the polymeric beads. Furthermore, the water is desorbed from the resin using a nitrogen gas desorption column at 113°C. The details of this pre-treatment and its specific conditions are provided to the reader in Appendix C.

In the first part of the impregnation process, the MNP coated with oleic acid is synthesised according to the proposed reaction conditions in Appendix A. A ferrofluid is synthesised by mixing 0.5 gr of MNP coated with oleic acid in 25 ml toluene. The mixture is sonicated for 1 hour. In this step, the flask top

is covered with a cap to prevent toluene from evaporating. The temperature of the bath is maintained at 20 °C. Once the ferrofluid is produced, it is advised to filter the ferrofluid by available syringe sieves with a size exclusion of 20 nm. By expelling the syringe's content, the ferrofluid becomes free of any agglomerated forms of MNP.

2.5 grams of PS/DVB beads are added to the flask for impregnation. We intend to limit the maximum possible ratio of MNP to beads below 1:5. A higher inclusion of MNP will reduce the adsorptive capacity of the beads. The beads are added to a flask and placed inside a sonification bath for 15 minutes. During this step, the resins swell, and impregnation starts.

Figure 3.2, the rotary evaporator laboratory setting with a heating bath containing a flask.

Table 3.4, Mass scale of components used in the dry impregnation experiment.

Mass of MNP	Mass of PS/DVB	Volume of the solvent	Duration of dry impregnation
0.50 gr	2.50 gr	25 ml	5 hrs

The mixture is initially preheated to 80°C, and vacuum conditions are slowly introduced. This pre-treatment is necessary to prevent turbulent evaporation of toluene due to the sudden release of trapped air inside the resins under vacuum conditions. This detrimental effect may cause the particles and the resins to leak into the condenser and complicates the process. Once the 230 mbar pressure is reached by ramping down the pressure, the rotary evaporator operates at a fixed temperature of 80°C with the suggested set point and threshold.

Table 3.5, Operational temperature, and pressure for impregnation of PS/DVB with MNP.

Temperature (T)	Pressure (P)	Excessive pressure (dP)	Duration
25 - 80 °C	1000 - 230 mbar (~100 mbar reduction every 7.5 minute)	60 mbar	1 hr
80 °C	230 mbar	60 mbar	4 hr
50 °C	100 mbar	25 mbar	1 hr

In the final step of the impregnation process, the temperature is adjusted to 50°C degrees and pressure is reduced to 100 mbar with excessive allowable pressure of 25 mbar. This final drying stage is prolonged for 1 hour to completely deswell the impregnated resins.

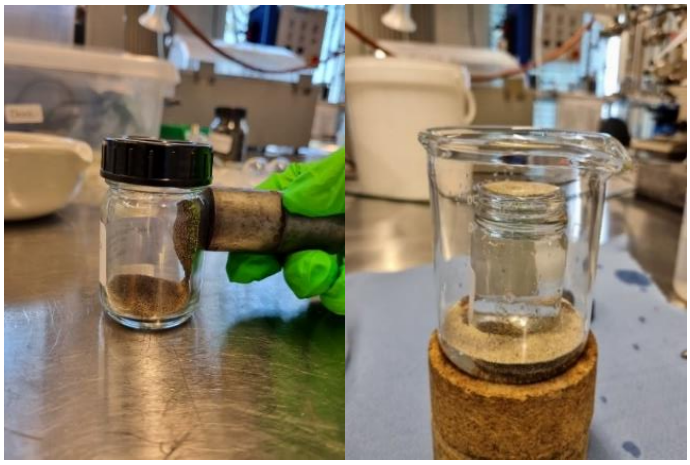

Figure 3.3, Interaction of impregnated resins with a static magnet.

In the last step of the process, a physical separation step is introduced to wash the resins from MNP that did not diffuse into the resins. This separation method exploits magnetic and buoyancy forces. The PS/DVB resins have a lower density than water; thus, they float on top of liquid water. On the other hand, MNP are denser and sit at the bottom of a flask containing water. Additionally, MNP have a higher affinity toward a static magnet than impregnated resins. These differences in physical properties are used for separation.

Initially, the flask's content detached from the rotary evaporator is placed inside a 50 ml open bottle. The bottle is placed inside a wider beaker which sits on top of a static magnet. In this separation, demi-water is slowly added to the bottle. As the water level inside the bottle rises, the impregnated resins start to flow to the top layer of the aqueous solution while the MNP separates from the resins and gets attached to the bottom of the bottle due to their stronger affinity to the magnet and lower buoyancy force. Furthermore, by allowing the bottle's content to overflow, impregnated resins are separated from MNP.

Afterwards, the resins are treated in a desorption column using heated nitrogen at 103°C. The treatment with nitrogen facilitates the removal of water content inside the pores and removes fine particle MNP that may remain on the resin's external surfaces.

3.2.2 Impregnation at normal conditions

Similarly, embedding MNP inside PS/DVB is attempted by simply allowing equilibrium to take place in an open flask containing ferrofluid and the PS/DVB resins. In this method, vacuum conditions and high temperatures are not applied. In contrast, the impregnation of MNP on PS/DVB occurs under atmospheric pressure and controlled laboratory temperature. For this approach, 1 g of PS/DVB is mixed with 10 ml of ferrofluid with a similar concentration of 20 g/l of MNP. The flask's lid is left open, and the ferrofluid is left under the laboratory hood to evaporate over days.

3.2.3 Adsorption of VFA from artificially made fermented wastewater

The adsorption capacity, isotherm, and rate of the impregnated (intensified method) and unimpregnated resins are measured and compared in batch and zero-length adsorption experiments. In these experiments, a mixture representing fermented wastewater is utilised, and the model aqueous solution is synthesised artificially. This stream is represented by four VFA (butyric acid (HBu), propionic acid (HPr), lactic acid (HLa), and acetic acid (HAc)) and three mineral salts (potassium chloride, sodium sulphate and sodium phosphate dibasic). For analysis, high-pressure liquid chromatography (HPLC) and ion chromatography (IC) are each used to measure the concentration of VFA, mineral acids and ions in the aqueous phase before and after each experiment. These measurements are crucial in obtaining equilibrium isotherms and calculating the adsorptive rate and capacity of the original and impregnated resins.

HPLC provides a normal distribution of an individual VFA concentration in the mobile phase at a specific retention time. This distribution is obtained by radiating the mobile phase with ultraviolet and visible light and appraising the output signal of the equipment. These signals consist of a UV-vis spectrum or refractive index parameter over various retention times. Moreover, the integral of peaks observed at these signals at specific retention times are calibrated with the weight concentration of different VFAs and mineral acids. By this approach, their weight fractions are measured. Information regarding the calibration procedure and the equipment are available in Appendix E. Similarly, the conductivity of the mobile phase is monitored over time for analysing the ion concentration in IC. At specific retention windows, the integral of peaks observed in the output signal is calibrated with different ions expected to be present in the aqueous solution. The equipment details and calibration lines for relevant cations and anions present in the artificially made fermented wastewater are provided in Appendix F.

For adsorption studies on fermented wastewater streams, an artificial aqueous solution is produced. This type of stream is diluted in VFA while it is rich in minerals. Typical fermented wastewater contains VFA, salts, trace metals and other compounds in Table 3.6 [5]. Previously it has been shown that salts and trace metals present in such streams have a negligible effect on the adsorptive capacity of non-functionalised PS/DVB adsorptive beads [5]. Furthermore, of all the possible mineral acids, only phosphoric acid can adsorb on the PS/DVB resins significantly.

Table 3.6, Compounds available in fermented wastewater.

Compound name	concentration / (g/l)	chemical formula
acetic acid	2.5−10	CH_3COOH
propionic acid	2.5−10	CH_3CH_2COOH
butyric acid	2.5−10	$CH_3(CH_2)_2COOH$
lactic acid	2.5−10	$CH_3CH(OH)COOH$
sodium	1-5	Na^+
potassium	1-5	K^+
chloride	1-10	Cl^-
phosphate	1-10	$H_2PO_4^-, HPO_4^{2-}$
sulfate	1-10	SO_4^{2-}
sulfide	0.3	S^{2-}
magnesium	0.3	Mg^{2+}
calcium	0.3	Ca^{2+}
ammonium	0.1	NH_4^+
Trace elements (e.g., cobalt, nickel, and iron)	10^{-4}	Co, Fe, Ni Ionic forms
Inert COD (e.g., humic acid and fulvic acid)	1	-
microbes	-	-

A concentrated version of the artificial fermented wastewater is produced by mixing VFA and mineral salts to represent this industrial downstream in extreme conditions. This version is diluted with milli-q water to produce additional equilibrium points for the batch adsorption experiments. More information regarding the actual mass of the concentrated and diluted versions are available in Appendix D. In this Appendix, information about the dilution factor required to reach the sensible range of measurement by IC is also provided. The artificially made concentrated wastewater has the following VFA and mineral content given in Table 3.7 and Table 3.8.

Table 3.7, VFA content of concentrated artificial fermented wastewater mixture [5].

Compound name	mass fraction / (wt. %)	pKa	standard density / (g/ml)
acetic acid (HAc)	1.25	4.76	1.049
propionic acid (HPr)	1.25	4.88	0.990
butyric acid (HBu)	1.25	4.82	0.964
lactic acid (HLa)	1.25	3.86	1.209

Table 3.8, Salt content of concentrated artificial fermented wastewater [5].

Compound name	Molecular formula	concentration / (mol/L)	mass percentage / (wt. %)	Mw / (g/mol)
Potassium chloride	KCl	0.25	1.86	74.55
Sodium sulphate	Na_2SO_4	0.25	3.55	142.04
sodium phosphate dibasic	Na_2HPO_4	0.50	7.09	141.96

3.2.4 Batch adsorption experiment.

By applying batch adsorption experiments, adsorption isotherms and the capacity of the impregnated resins (intensified method) at 25°C and atmospheric pressure are measured and compared with non-impregnated resins. This experiment investigates multi-component compounds' adsorption from artificially made fermented wastewater. By utilising the concentrated and diluted versions of the

artificially made fermented wastewater, it is possible to operate the batch adsorption from different initial concentrations and eventually reach points on an isotherm for each compound.

The flasks used for these experiments are 20 ml in volume. During the batch adsorption experiment, they are maintained inside an isothermal shaking bath overnight. The condition inside this equipment is 25°C and atmospheric pressure, and the mixing rate is set to 120 rpm.

Inspired by precedent batch adsorption experiments on diluted streams [5], [39], [40], in each flask, approximately 300 mg of impregnated resin or non-impregnated resins is brought in contact with 10 gr of solution at different dilutions. Overnight the solid and liquid phases equilibrate. When the equilibrium is achieved by applying Equation (3-1) and using analytical measurement tools, the isotherm for each compound is calculated and graphically shown.

$$q_i = \left(x_{0_i} - x_{e_i}\right) \frac{W_l}{W_s(1-y_{mnp})} \tag{3-1}$$

The concentration of VFA and mineral acids are obtained using HPLC, while the concentration of ions is obtained with IC. It is possible to measure the amount adsorbed into the impregnated or non-impregnated resins by making a mass balance according to Equation (3-1). In this equation, the initial mass fraction of compounds in the liquid phase before and after equilibrium are measured and subtracted. In this equation, x_{0_i} and x_{e_i} denotes the initial and equilibrium weight fraction of each compound in the aqueous liquid phase. W_l and W_s each stand for the weight of the liquid and the resin.

The measurement of the MNP weight fraction (y_{mnp}) is done using atomic absorption spectroscopy. The parameter q represents the adsorptive capacity of compounds per mass of impregnated or non-impregnated resins.

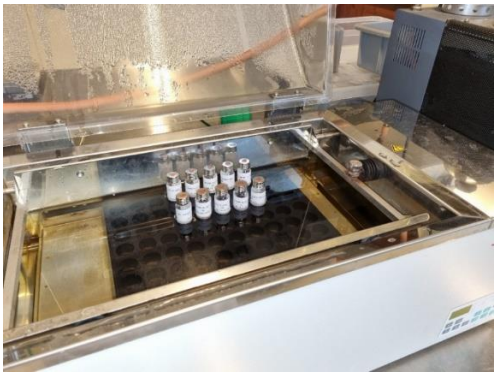

Figure 3.4, Batch adsorption experiment in shaking bath at standard conditions.

3.2.5 Zero length column adsorption experiments

The adsorption kinetics of compounds on spherical resins packed in a column is influenced by the axial dispersion of compounds in the fluid phase, film layer resistance between the fluid and solid phases, and intraparticle diffusion inside the solid adsorptive beads [41]. It is possible only to evaluate the effect of intraparticle diffusion and isolate it from the rest of the mass transfer phenomena by conducting a zero length column experiment [42]. In this setting, the column length is chosen to be as close as possible to zero (approximately: 8 mm [43]). Consequently, axial dispersive effects are rendered negligible. Furthermore, the fluid flow rate inside the column is maintained sufficiently high to prevent the accumulation of adsorbates in the liquid phase close to the interface of the solid and liquid phase;

consequently, boundary layer mass transfer limitation becomes minimal. Under such experimental circumstances, the determining mass transfer regime is diffusion inside the spherical spheres that control the overall adsorption kinetics.

A ZLC experiment is conducted to investigate the effect of the MNP coating of the impregnated resins on the adsorption kinetics of VFA. Additionally, the results of this experiment can be interpreted to obtain adsorbate diffusivity coefficients [42], [44].

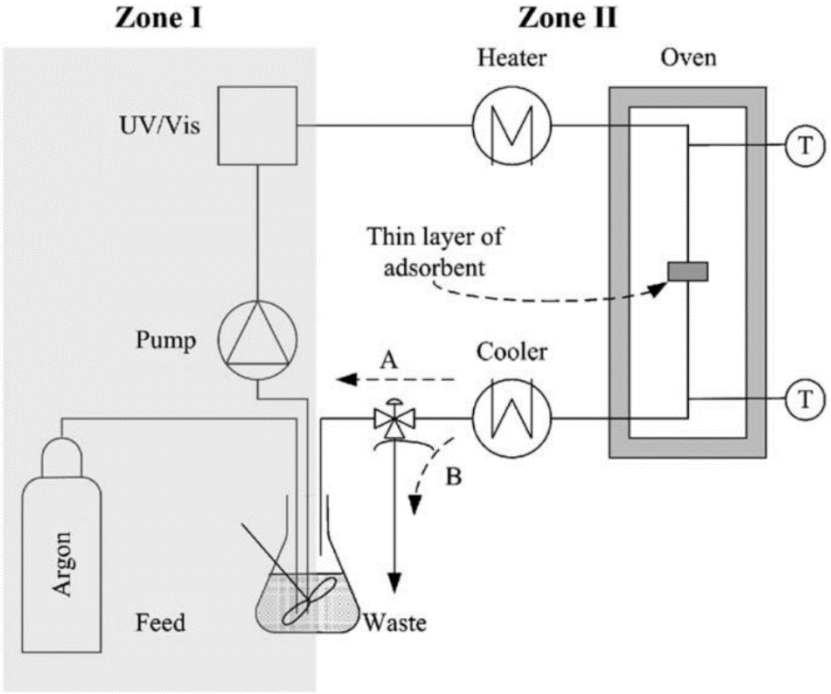

Figure 3.5, General schematics of a ZLC experiment [45].

The configuration of this experiment, as shown in Figure 3.5, involves two zones. From the first zone, artificially made fermented wastewater solution is pumped into the adsorption compartment, where a thin adsorbent layer is fixed inside the zero-length column. The outflow of the second zone is recycled to the initial solution and stirred. Subsequently, the concentration of various adsorbing compounds is monitored throughout the experiment.

In the ZLC experiments, the impregnated resins via the intensified conditions are compared with the original resins. In an ideal setting, they are locked within this height via plungers located at the top and bottom of the ZLC column. This relatively small height is significant because axial dispersion effects are negligible under this condition. Thus, the outlet concentration of butyric acid is equal to the concentration of the liquid phase at equilibrium with the adsorbed butyric acid on the resin. Furthermore, the outlet concentration is monitored throughout the experiment using HPLC and IC samples. These samples are analysed to measure the diffusivity coefficient of HBu and HPr.

Inspired by previous experiments, the following settings are implemented in the ZLC experiment. The variables are chosen to obtain a 10% reduction of HBu concentration at the end of the experiment.

The diffusivities of adsorbing compounds in a ZLC experiment is obtained by fitting the desorption curve with a diffusion-controlled asymptote solution provided for conventional ZLC experiment [44]. The diffusion-controlled asymptote ($L >> 1$) case only contains the first term of the general summation solution given in Equation (3-2). The linearised data obtained from the ZLC experiments are fitted with

the first term of Equation (3-2) while considering the definition and boundary of L given by Equation (3-3). Thus, β_1 and D are both obtained from the ZLC results.

$$\frac{C}{C_0} = 2L \sum_{n=1}^{\infty} \frac{1}{\beta_n^2 + L(L-1)} e^{\left(-\frac{\beta_n^2 tD}{R^2}\right)} \tag{3-2}$$

$$L = 1 - \beta_n \cot \beta_n \tag{3-3}$$

3.2.6 Hyperthermia experiment

In hyperthermia studies specific absorption rate (SAR ($\frac{W}{kg}$)) is measured in an experimental setting. In this study, a sample is influenced by an AMF with a frequency of 52 kHz and a magnetic amplitude of 25 mT. While the sample is under the influence of the external AMF, its temperature is monitored continuously by using a thermal probe with a non-metallic liquid indicator.

The small sample volume is chosen to be relatively small, approximately 1 ml. The sample is kept inside an insulated cylindrical tube in which heat loss to the external walls of the column is negligible. In these hyperthermia studies, the column contains either a liquid phase with MNP or a mixture of a liquid phase with solid impregnated resins.

An example of the column containing the beads and the liquid phase is graphically shown in Figure 3.6. By using image processing applications (draw.io), the column liquid hold up is measured to be 0.6 (ε_l).

In this hyperthermia study, the temperature of the sample inside the column is monitored over time. An energy balance over the sample elucidates the dynamics of heat transfer under the influence of an AMF. With regards to this energy balance, a few assumptions are made:

- Evaporation of the liquid phase does not occur.
- Heat diffusion into the insulated walls of the column is negligible.
- The mixture medium resembles a lumped system.
- Uniformity of temperature between the liquid and solid phase of the sample

Figure 3.6, a mixture of ethanol (1 ml) and impregnated (at intensified conditions) PS/DVB resins (0.2 g) inside the column sample.

The energy balance includes heat production of MNPs (Q_{SAR}), and heat losses due to heat convection to the air above the liquid interface. The complete energy balance based on the previously mentioned assumptions is Equation (3-4).

$$\left(\varepsilon_s C_{p,s} + \varepsilon_l C_{p,l}\right)\frac{d\left(T-T_{ref}\right)}{dt} = Q_{SAR} - \frac{UA}{\rho V}(T - T_\infty) \tag{3-4}$$

In the initial moments of the hyperthermia experiment, heat losses due to convection are negligible because the sample is in equilibrium with its surrounding air at the beginning of the experiment. Thus, at the initial conditions of the experiment, the energy balance is reduced to Equation (2-2), in which the specific heat of the mixture is used. Therefore, it is possible to measure the SAR by considering the initial slope of the medium temperature profile under the influence of AMF. The equipment producing the AMF is shown in Figure 3.7. This device utilises a current of 12.85 A and a voltage of 24.50 V to produce an AMF of 25 mT with a frequency of 52 kHz by incorporating a solenoid.

Table 3.9, Hyperthermia experimental setting.

Parameter	Value
AMF amplitude	25 mT
AMF frequency	52 kHz
Mass of resin (if applicable)	200 mg
Volume of liquid	1 ml

Figure 3.7, the external AMF for the hyperthermia studies is produced by solenoid.

3.3 Numerical method

A numerical diffusion model for finite spherical mediums is introduced to investigate the impregnation process of PS/DVB with MNP suspended in a slowly evaporating toluene solvent.

3.3.1 Mathematical formulation

The diffusion of MNP from solvent into swollen spherical PS/DVB resins during diffusional impregnation is represented by an unsteady-state diffusive partial differential Equation (PDE) (3-5) over a spherical control volume that resembles the porous resin (*res: inside the internal crosslinked polymeric structure, org: organic solvent*). The parameter C denotes the concentration of MNP in liquid or solid phases.

$$\frac{\partial C_{res}}{\partial t} = D\frac{\partial^2 C_{res}}{\partial r^2} + \frac{2D}{r}\frac{\partial C_{res}}{\partial r} \tag{3-5}$$

In this mathematical model, the following assumptions are made:

- The resins are considered spheres with a uniform density, porosity, tortuosity, and pore size.
- The diffusivity of the MNP is constant.
- MNP distribution coefficient (m) between the resin and the organic solvent phases is 1.
- The liquid phase outside of the porous resins is ideally mixed
- External boundary layer mass transfer limitation on the resins is negligible.
- The vacuum system is kept at a constant temperature.
- Evaporation continues at a constant rate.

The PDE describing the impregnation process has the following boundary conditions:

$$r = 0, \qquad \frac{\partial C_{res}(t,0)}{\partial r} = 0, \qquad 0 < t \tag{3-6}$$

$$r = R, \qquad C_{res}(t,R) = m\, C_{org}(t), \qquad 0 < t \tag{3-7}$$

$$t = 0, \qquad C_{res}(0,r) = 0, \qquad 0 \le r < R \tag{3-8}$$

Equation (3-7) describes the boundary condition at the external surface of the spheres. Over time as the organic solvent evaporates and the MNP diffuses into the resin phase, the concentration of the organic phase changes; hence the boundary condition also changes. Any numerical approach must update the boundary condition accordingly.

A total mass balance of MNP, which includes all nanoparticles that have either diffused into the resin or are still contained by the organic solvent phase within the system, is shown in Equation (3-9). Furthermore, by assuming a constant evaporation rate of the organic solvent over time, Equation (3-10) calculates the changing boundary condition of the PDE. It is assumed that the volume of the organic phase evaporates at a constant rate. In the case of impregnation in a non-evaporative system, the evaporation rate term (ΔV_{org}) is be set to be zero.

The amount of MNP diffused into the resin is averaged numerically by Equation (3-11). Substituting all the previous equations into one relation for the concentration of MNP in the organic phase is given in Equation (3-12).

$$M_{tot} = M_{res} + M_{org} \tag{3-9}$$

$$C_{org}(t) = \frac{M_{org}}{V_{org}} = \frac{M_{tot} - M_{res}}{V_{org_0} - \Delta V_{org}\, t} \tag{3-10}$$

$$M_{res} = V_{res}\, \overline{C_{res}(t)} \tag{3-11}$$

$$C_{org}(t) = \frac{M_{tot} - V_{res}\, \overline{C_{res}(t)}}{V_{org_0} - \Delta V_{org}\, t}\ ,\ 0 < t,\ \varepsilon V_{res} \leq V_{org} \tag{3-12}$$

In Equation (3-12), the mass of diffused MNP inside the resin is approximated by using the following averaging scheme in Equation (3-13) [41].

$$\overline{C_{res}(t)} = \frac{3}{R}\int_{r=0}^{r=R} r^2 C_{res}(t,r)\ dr \tag{3-13}$$

As indicated by the concentration profile of MNP in the organic phase in Equation (3-12), this derivation applies until the volume of the organic solvent equals the pore volume of the resin ($\varepsilon V_{res} \leq V_{org}$). At this critical limit, the impregnation regime changes from diffusional to capillary. In this case, in which the deswelling of the resin occurs, at capillary impregnation, additional MNP is not introduced into the resins; rather, their distribution and withdrawal are affected by the evaporation rate of the solvent. Thus, according to the definition for the MNP concentration in the organic solvent, this numerical approach sufficiently solves the diffusional impregnation of the resins. The final stage of impregnation, referred to as capillary impregnation, is dominated by capillary forces at interfacial surfaces within the crosslinked internal structure of the resins. Furthermore, a simulation at this level must consider the inhomogeneous concentration of MNP in the solvent occupying the external boundary layer and the internal pore volume of the resin. This can only be done by applying a molecular dynamic simulation.

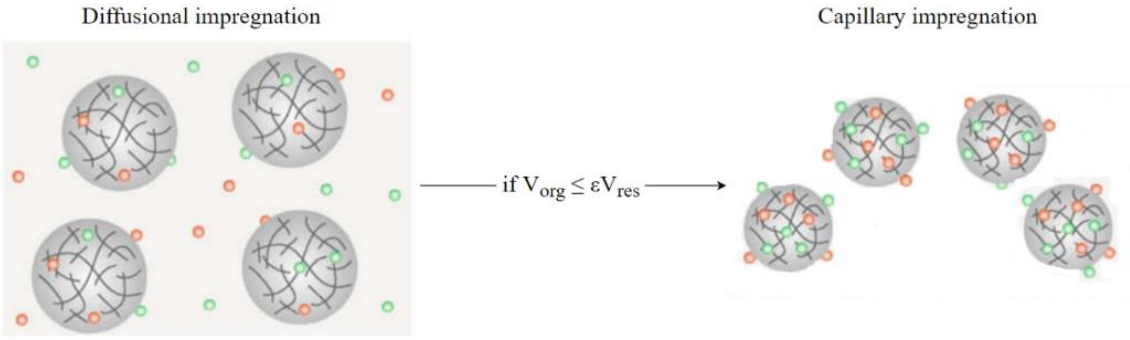

Figure 3.8, Change of impregnation regime as solvent evaporates.

At the beginning of the capillary impregnation, the resins contain all the remaining organic solvent, and no external solvent is available on the surface of the resins. Nevertheless, there will be solid MNP loosely bound to the resins' outer adsorptive surface.

3.3.2 Numerical approach

To solve this PDE numerically, the radius and the time variables needs to be discretised in a numerical domain. Since on the right-hand side of the PDE (3-1), the coefficient of the first derivative of MNP concentration inside the resins with regards to the radius ($\frac{\partial C_{res}}{\partial r}$) is a reciprocal function of radius ($\frac{2D}{r}$), numerical solutions for different step-sizes of radius (Δr) do not converge toward a general solution. This occurs because at the right-hand neighbourhood of zero in the radius domain, this coefficient becomes larger as the discretised radius reaches the limits of zero. The large diffusivity neglects the physical size limitations of the diffusing particle and hence produces unrealistic results. To tackle this numerical issue, Equation (3-5) is modified by employing a variable substitution [46]. By using the substitute variable ($u = C_{res} r$), Equation (3-5) is transformed into Equation (3-14).

$$\frac{\partial u}{\partial t} = D \frac{\partial^2 u}{\partial r^2} \tag{3-14}$$

The boundary conditions are transformed accordingly to the following:

$$r = 0, \quad u = 0, \quad 0 < t \tag{3-15}$$

$$r = R, \quad u(t, R) = mR\, C_{org}(t), \quad 0 < t \tag{3-16}$$

$$t = 0, \quad u = 0, \quad 0 \leq r < R \tag{3-17}$$

The substituted PDE in Equation (3-14) is discretised in time and space domains. An explicit Euler time advancement scheme is implemented for the time domain, while a central discretisation scheme is used for the second derivative of concentration with regards to the radius. The numerical solution obtained via this numerical approach is compared and evaluated with the reference book, *'The mathematics of diffusion by Prof. J. Crank'*, suggesting the substitution approach [46]. Subsequently, it is used to study the MNP concentration profile after the impregnation when the diffusivity of MNP is varied from 10^{-11} to $10^{-15}\,\frac{m^2}{s}$.

3.3.3 Numerical model validation with an asymptote analytical solution

The reference book provides a general solution for the PDE representing the unsteady state particle diffusion into a finite spherical medium [46]. This general solution is analytically solved for a case in which the boundary concentration of MNP in the liquid organic phase is constant during the duration of the diffusional impregnation. The developed numerical model reflects this condition when the volume of the liquid phase is much larger than the volume of the resin and when the evaporation rate of solvent (ΔV_{org}) is zero. Under these conditions, diffusion of the MNP from the liquid phase to the resin phase will have a negligible effect on the concentration of MNP in the organic liquid phase. Thus,

it is possible to compare the numerical and analytical methods under these conditions. The result of the numerical method under the mentioned conditions is checked with the general analytical solution to validate the numerical approach.

The result of the implemented numerical method is simulated and compared with the general solution in Figure 3.9. The general analytical solution is provided on the left side, and it is based on a dimensionless parameter incorporating diffusivity (D), duration of diffusion (t) and the radius of the spheres (a or R). The numerical solution at the same conditions is provided on the right side of Figure 3.9.

By analysing Figure 3.9, a similar concentration profile to the analytical profile of MNP diffusion into PS/DVB resins is obtained from the numerical approach. Thus, the analytical and numerical methods concur with each other. Specific to the impregnation case, the numerical approach is extended to incorporate solvent evaporation effects while a lower amount of solvent is used during the process. This numerical method is applicable for scale-up and optimisation purposes. Using this numerical model, it is also possible to calculate the diffusivity of MNP into PS/DVB during the impregnation.

In Figure 3.10, the iterative method is visually summarised. In this explicit method, the concentration of the boundary layer is updated in each iteration. Once the solvent volume is reduced below the critical volume of the resin, the impregnation regime is changed from diffusional to capillary. Compared with the analytical method, the changes in organic phase concentration are much lower under the proposed conditions. Furthermore, since evaporation does not occur, a transition into the capillary impregnation regime does not occur. Hence the comparison between the results are valid.

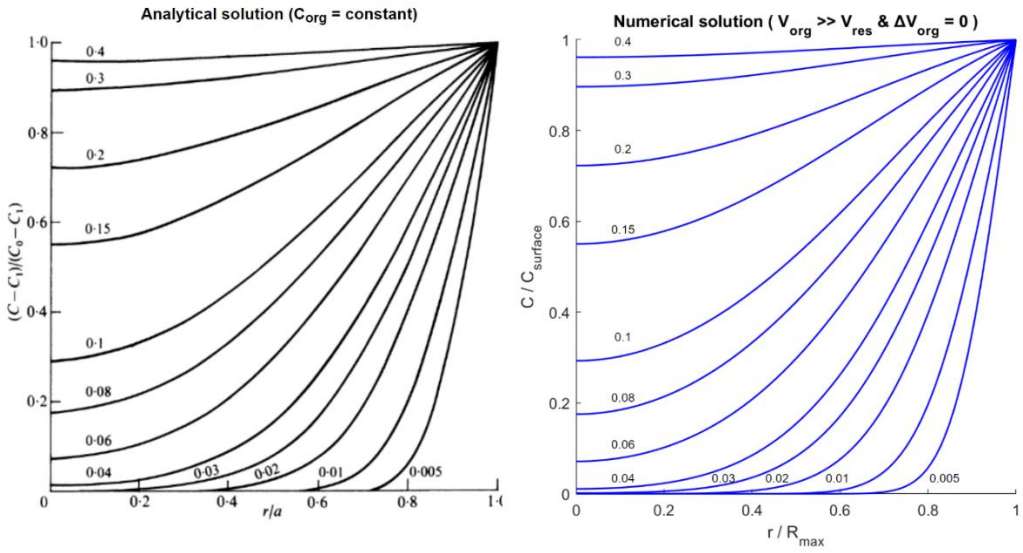

Figure 3.9, Comparison of the numerical result with analytical solution [46]. Numbers on the graph represent ($\frac{Dt}{a^2}$ or $\frac{Dt}{R^2}$). The initial concentration in the sphere is set to be zero.

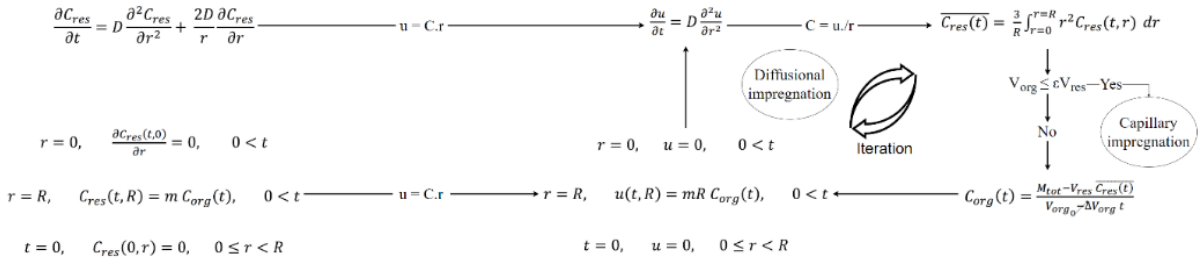

Figure 3.10, The iterative numerical method for calculating the amount of diffused MNP.

Chapter 4: Results

After the impregnation process via the intensified and normal methods, the colour of PS/DVB resins changed from white into a spectrum of colours ranging from yellow to brown and black. This change of colour is a visual confirmation of PS/DVB impregnation with MNP.

The impregnated resins are evaluated via analytical methods such as s atomic absorption spectroscopy (AAS) and scanning electron microscopy (SEM). Accordingly, a diffusivity coefficient for MNP is calculated by comparing the analytical and numerical results. Furthermore, the adsorptive and hyperthermia capabilities of the impregnated resins are evaluated.

Impregnation by the normal condition method took 15 days. In that period, 10 ml of toluene was evaporated under normal conditions. Compared to the intensified method, the resultant product is impregnated with resins with magnetic properties and has a homogenous dark brown colour.

Figure 4.1, Visual confirmation of impregnation via intensified method by griding the particles.

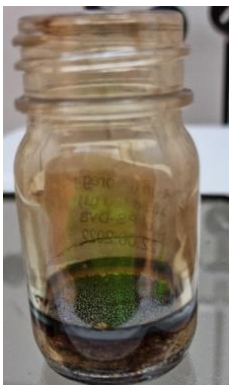

Figure 4.2, Impregnated resins via normal method after 15 days being left with an open flask.

4.1 Experimental results

Two analytical approaches are utilised to decipher more about the MNP content of the impregnated resins. The total mass of MNP incorporated into the impregnated PS/DVB resins (both method) is calculated through AAS. Furthermore, by applying SEM on cut impregnated resin (intensified method) samples, the radial distribution of the MNP inside the resins and its distribution external to the surface of the impregnated resins are evaluated.

4.1.1 MNP impregnated resins analysis via atomic absorption spectroscopy

The mass of coated MNP diffused into the impregnated resins is measured through elemental analysis of metallic cations of iron via atomic absorption spectroscopy. This analysis utilises atomic absorption spectroscopy (AAS) of digested magnetite nanoparticles in strong mineral acid.

The unique electronic structure of most metallic elements causes the absorption of radiated light from a source with a pre-defined wavelength to be element specific. As a result, the mass of iron content inside a sample is measured using a calibration line correlating the absorbance with iron concentration. The calibration line correlating absorbance with the concentration of iron is provided in Appendix G.

The coated magnetite is made from oleic acid surfactant surrounding iron and oxygen atoms that are organised in a crystalline structure. The ratio of oxygen atoms to iron atoms inside the structure is 4:3. Thus, by knowing the mass of iron atoms within the structure, it is possible to calculate the corresponding mass of oxygen atoms in the crystalline packing and thus the total mass of MNP. To fully convert the mass of iron into the mass of coated MNP, an additional parameter besides the ratio of oxygen atoms to iron atoms is required. This parameter is the mass ratio of oleic acid surfactant to the mass of MNP.

For this reason, a sample with a known weight of coated MNP is dissolved in highly concentrated acid. This solution can hydrolyse the magnetite into iron cations. The preferred acids for this purpose are strong mineral acid solutions such as nitric acid [47] or a mixture of nitric acid and hydrochloric [48].

10.9 mg of coated MNP is hydrolysed with a highly concentrated acidic solution of 3.6 ml hydrochloric acid (36 wt.%) and 1.2 ml nitric acid (69 wt.%). This solution is heated and mixed using a magnetic stirrer at 230 rpm at 60°C for 3 hours. Afterwards, it is diluted by adding 1 ml of the acidic solution into 40 ml of milli-q water. The diluted solution is analysed using AAS, and the corresponding result is given in Table 4.1.

Table 4.1, AAS result of coated MNP.

Parameter	Value
Mass of sample (mg)	10.9
Volume of acidic solution (ml)	4.8
Dilution factor	0.02439
Absorbance (Au)	0.1462, 0.1471, 0.1493
Average concentration (ppm)	39.10
Mass of Fe (mg)	7.69
Mass ratio of MNP to Fe	1.3820
Mass of MNP (mg)	10.63
Mass ratio of coated MNP to MNP	1.025

The mass of oxygen atoms in the samples is calculated based on the mass of iron and combining both masses provides information regarding the mass of the crystalline structure. Furthermore, by knowing

the initial mass of the analyte, the mass ratio of surfactant to the magnetite is determined. This latter information is essential in calculating the mass of diffused coated magnetite into the PS/DVB resins.

Analysing the mass of MNP diffused into the PS/DVB resins via intensified and normal methods after the impregnation process is conducted similarly by first allowing the hydrolysis of coated MNP inside pores by the mentioned highly concentrated acidic solution. Then again, the solution is heated, mixed, and diluted.

The dilution in both cases is chosen to ensure the iron concentration is within the feasible measurement range. The AAS equipment measures more accurately when the aqueous solution's iron concentration is within a range of 1 - 100 ppm.

By analysing the impregnated resin made from both methods, the mass fraction of diffused coated MNP in resins made from both cases is measured and compared in Table 4.2.

Table 4.2, AAS results of the impregnated resins.

Parameter	Impregnated resin via intensified method	Impregnated resin via normal condition method
Mass of sample (mg)	34.0	30.3
Volume of acidic solution (ml)	4.8	4.8
Dilution factor	0.02439	0.02439
Average concentration (ppm)	6.06	16.5
Mass of Fe (mg)	1.192	3.247
Mass of MNP (mg)	1.648	4.487
Mass of coated MNP (mg)	1.689	4.599
Mass fraction of coated MNP (y_{mnp})	0.050	0.152

The fraction of diffused coated MNP into the PS/DVB resins (y_{mnp}) made from the normal method is higher than in the intensified method. This result indicates that increasing the impregnation duration by reducing the evaporation rate over time can significantly increase the MNP content of the impregnated resins. Nevertheless, under normal impregnation conditions, the diffusivity of MNP compounds into the polymeric matric is comparatively less than in intensified impregnation conditions.

In contrast, at the intensified impregnation method, 33% of the MNP diffusion achieved in the normal method is obtained in approximately 1.38% of impregnation duration under the normal conditions.

4.1.2 MNP impregnated resins analysis via scanning electron microscopy

SEM images of cut impregnated resin obtained via the intensified method are obtained to comprehensively analyse the radial distribution of MNP inside the PS/DVB resins and MNP distribution external on the PS/DVB surface after the impregnation. Initially, the embedded beads are cut using a sharp knife in a petri dish under a microscope. Then the samples are placed inside high-resolution SEM equipment. Three different regions are distinguishable from the magnified images given in Figures 4.3-4.7.

As is visible from Figure 4.3 and Figure 4.4, after the impregnation process, the external surface of the impregnated PS/DVB resins is fully covered with a diffused MNP layer which is enmeshment of polymeric structure and the diffused MNP. The layer has an average thickness of 1.5 μm. On top of this layer, especially on impregnated resins with a darker colour, agglomeration of magnetite nanoparticles is visible. This agglomerate is loosely adsorbed on the impregnated layer and is separable by employing physical force such as contacting it with a sharp knife, sonification or bringing it in contact with a flowing stream characterised by a high Reynolds number.

By this process, impregnation of MNP into the PS/DVB resins is only achieved close to the external surface of PS/DVB. The thickness of the outer layer varies from point to point but is within the range of 1-2 μm.

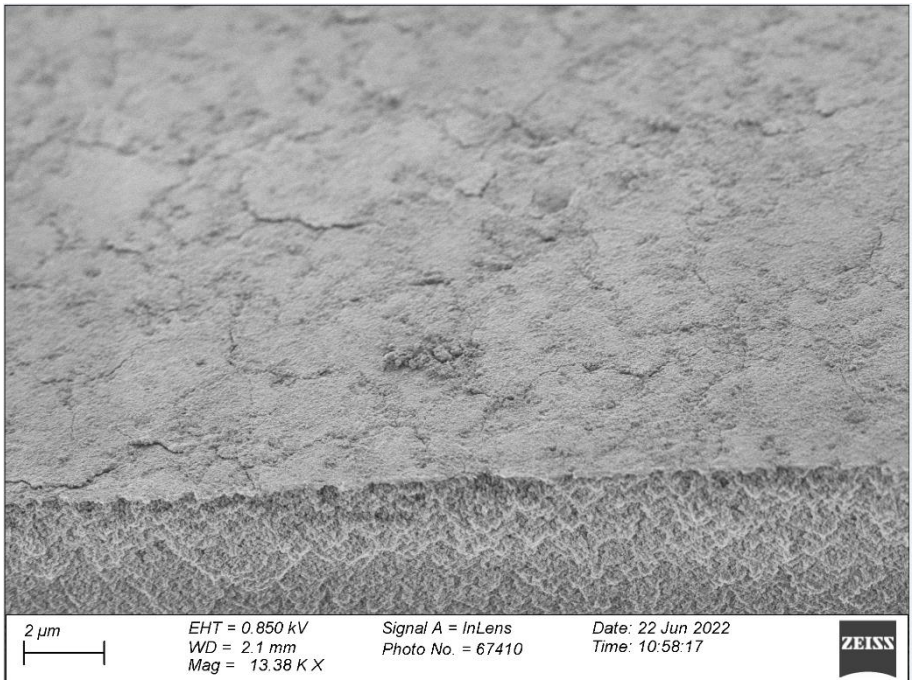

Figure 4.3, Total coverage of the external surface of the impregnated resin with an MNP coating.

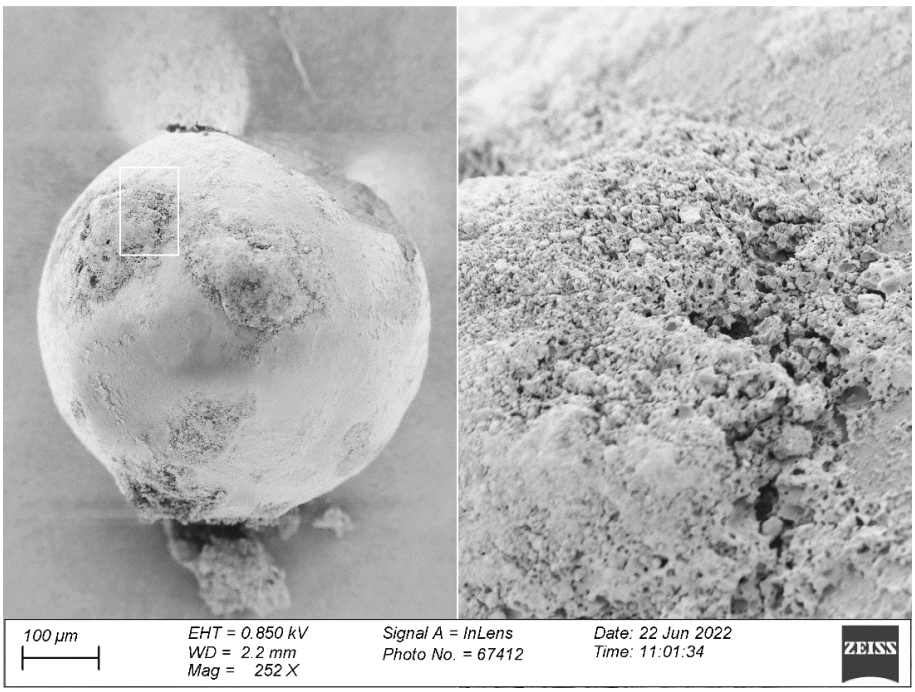

Figure 4.4, Agglomeration of MNP on top of the diffused MNP layer attributed to colour spectrum of impregnated resins

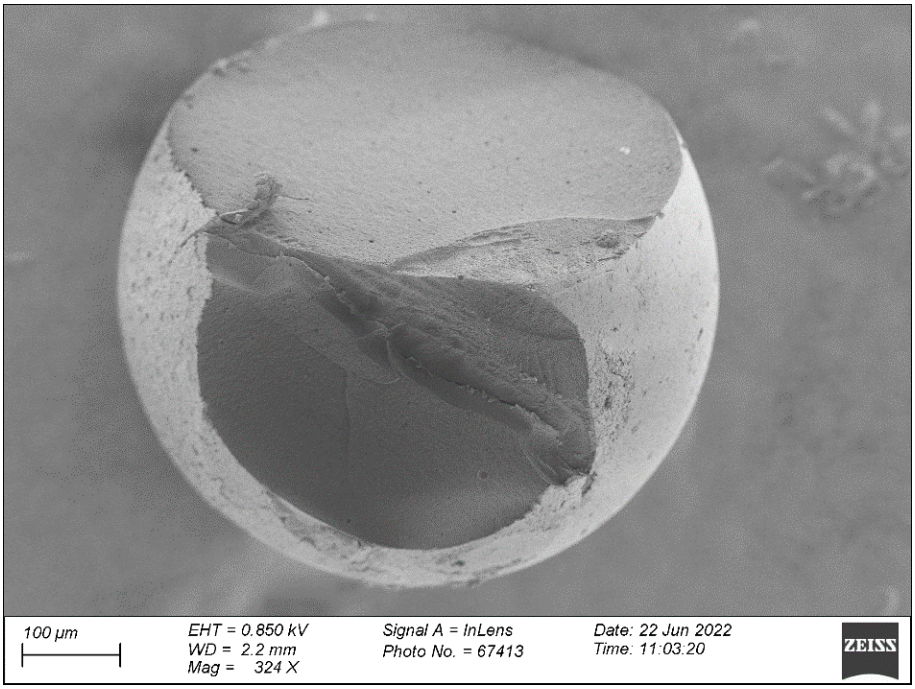

Figure 4.5, SEM image of a cut impregnated resin bead with no visible MNP close to the core of the resin.

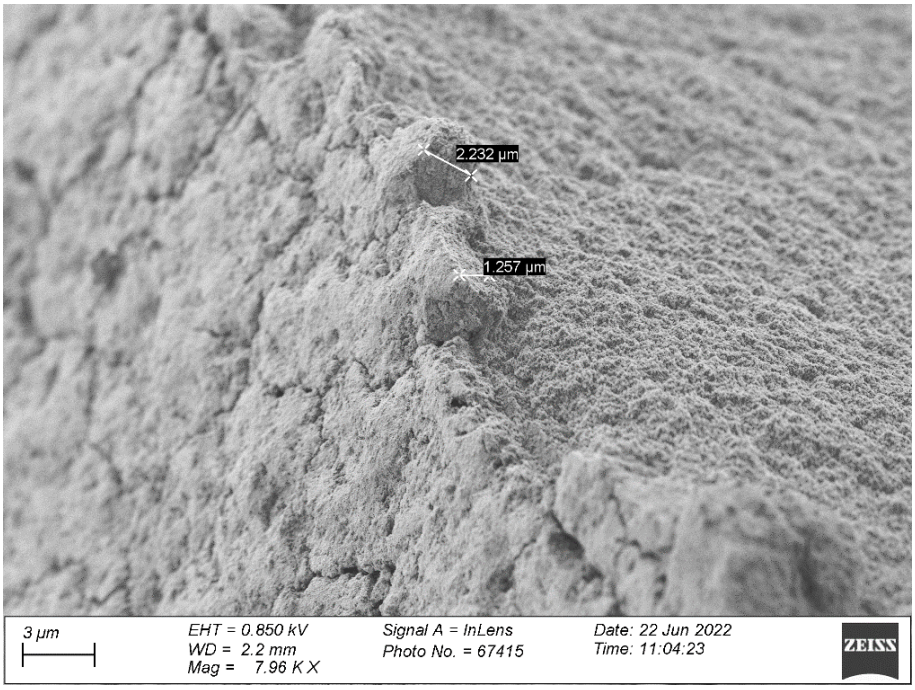

Figure 4.6, close-up image of the magnetite coating on the PS/DVB resins.

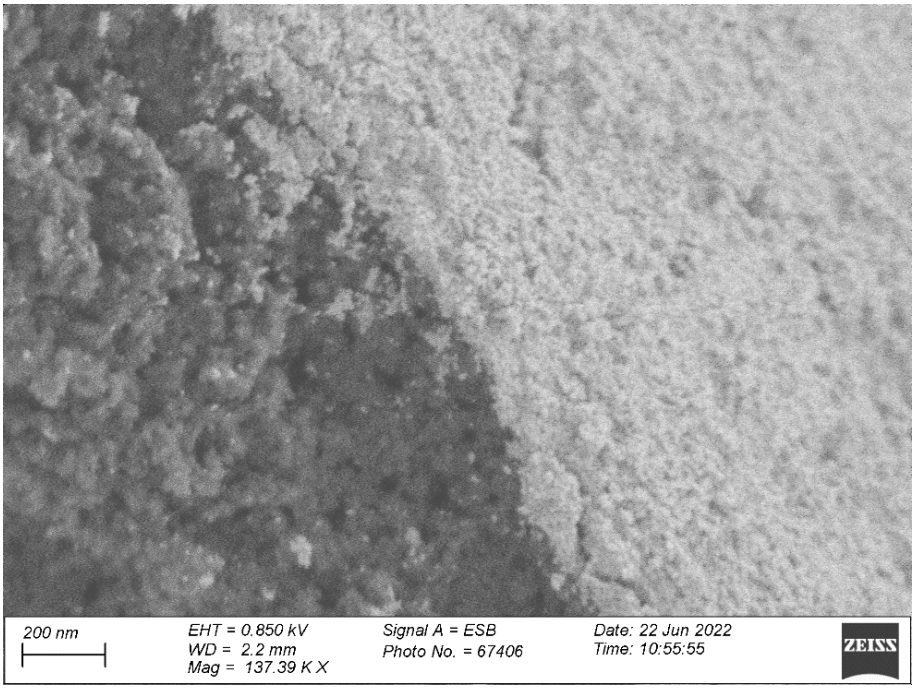

Figure 4.7, MNP farther away from the boundary layer.

In some instances, close to the boundary layer between the PS/DVB and the diffused MNP layer, sparse MNP compounds are visible inside the PS/DVB polymeric network (Figure 4.7). The SEM analysis shows that the total mass obtained from the AAS is not entirely contributed to the mass of MNP that has successfully diffused into the PS/DVB resins, but it also contains the agglomerate regions on top of the diffused MNP layer.

4.1.3 MNP leeching under sonication.

Instability of the diffused MNP layer in the PS/DVB resins occurred upon exposure to high pressures and turbulent flows characterised by a high dimensionless Reynolds number. Therefore, the currently prepared impregnated resins are unsuitable under turbulent flow regimes. Impregnated resins via both methods are sonicated for 1 hour to examine the extent of leeching under turbulent flow regimes. Afterwards, their MNP content is analysed via AAS. This analysis proved that almost all the MNP leeched out of the impregnated resins.

In contrast, introducing mixing conditions via vortex formation and rotation does not affect the MNP content of impregnated resins as much as sonication at high frequency. A literature search of the diffusion mechanism is conducted to elucidate the rapid leeching of MNP at high physical vibrations,

These observations regarding the leeching behaviour of nanoparticles in a highly vibrating environment are confirmed by a proposed activated hopping diffusion mechanism [49]–[51].

Crosslinked polymers are materials capable of absorbing and dampening sound waves [52]. It is hypothesised that energy absorption from sonication waves influences the external surface structure of the impregnated crosslinked polymers more predominantly than the network's internal structure. Thus, the polymeric surface of the network fluctuates more rapidly. As a result, the polymeric network's external pore (cage) structure - a crucial element in the hopping diffusion mechanism - changes faster than the internal one. Consequently, the activation energy for the polymer nanoparticle to leech out of the polymeric network structure is supplied while activated internal diffusion occurs less frequently.

Hence, this theory explains why the leeching of MNP happens so rapidly while it takes hours for MNP to diffuse into the PS/DVB matrix during the impregnation process.

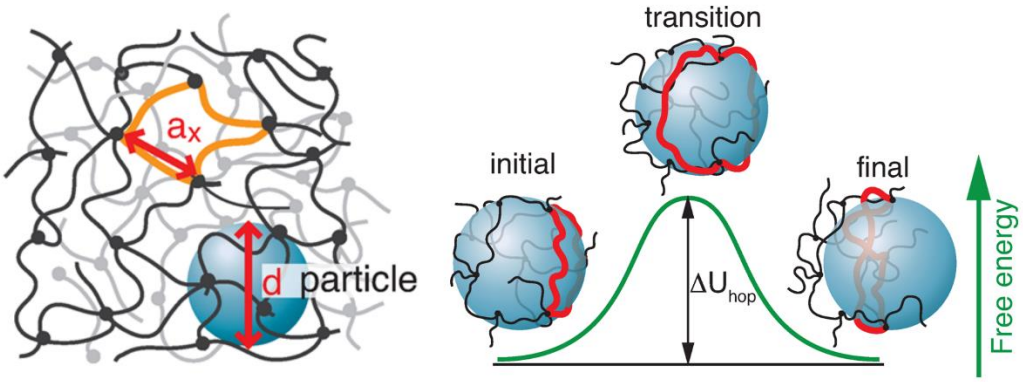

Figure 4.8, Hopping diffusion of nanoparticles through a untangled cross-linked polymeric matrix [50].

Figure 4.9, MNP leeching after and before sonication in milli-q water.

4.2 Numerical results

The previously formulated and validated discretised numerical method is utilised to simulate the impregnation process at the chosen experimental conditions. Based on a range of diffusivity coefficient, possible scenarios for the MNP concentration profile after the impregnation process is graphically shown. By translating the concentration profiles at different scenarios into a singular parameter defined as penetration depth, a means for calculating the numerical diffusivity of MNP into the PS/DVB resins is established.

4.2.1 Sensitivity analysis on MNP diffusivity coefficient

This numerical sensitivity analyses the impregnation of 2.5 grams of PS/DVB resins with 0.5 grams of MNP stably suspended in 25 ml of toluene. The impregnation duration of the mixture at vacuum conditions with a constant evaporation rate is set to 5 hours. By setting the mentioned variables into the numerical simulation, the effect of diffusivity is graphically presented in Figure 4.10. At different diffusivity levels concentration profile obtained inside the resin at the end of the impregnation process varies.

As shown by the numerical sensitivity analysis above, when diffusivity is low, the incorporation of MNP close to the external surface of the resins is more predominant. Thus, impregnation will only result in an external coating of the resins. Hence at low diffusivities, MNP will not reach the cores of the resins during the impregnation.

If the diffusivity of MNP is higher than $10^{-13}\ \frac{m^2}{s}$, based on the sensitivity plot in Figure 4.10, five hours of impregnation process is sufficient to get a sensible amount of MNP impregnated close to the core of the PS/DVB.

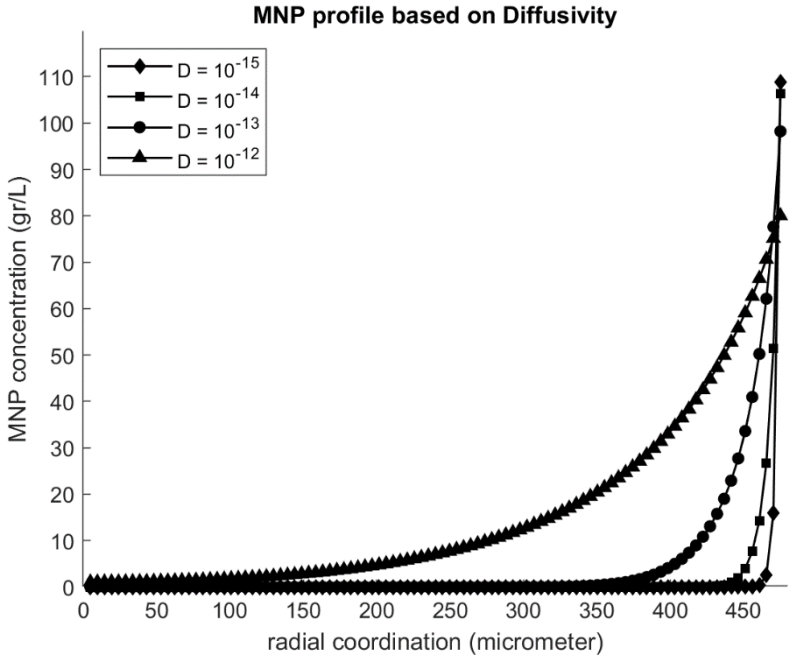

Figure 4.10, Final concentration profile inside an individual resin right after diffusional impregnation.

4.2.2 Calculation of MNP diffusivity coefficient

The mass of MNP obtained from AAS of impregnated resins includes the mass of agglomerate forms on the external surface and the mass of diffused MNP into the PS/DVB resin. Thus, obtaining a numerical correlation between the total mass and diffusivity of MNP is not a viable approach for calculating diffusivity based on the output of AAS. A more accurate approach is to base the calculation according to the depth of the MNP diffused layer, measured with SEM to be approximately 1.5 µm in the impregnated resins.

By assuming that at the end of the penetration depth, the concentration of MNP is lower or equal to 1% of the surface concentration, the penetration depth parameter is defined numerically. Nevertheless, this diffusivity is based on an ideal case and roughly estimates the real case scenario. Agglomerate formation on the external surface reduces the driving force of MNP to diffuse farther into the core of resins. Additionally, during the impregnation process, the rotary evaporator introduces mixing to the flask by rotating the flask. Hence, a centrifugal force is induced on MNP particles inside spherical resins. The effect of these forces on MNP diffusion introduces nonidealities that skew the MNP profile inside the particle to the external surface. Hence, a rough numerical approximation for diffusivity is measured by basing the calculation on the most diffusive MNP particles, which are closest to the end of the penetration depth.

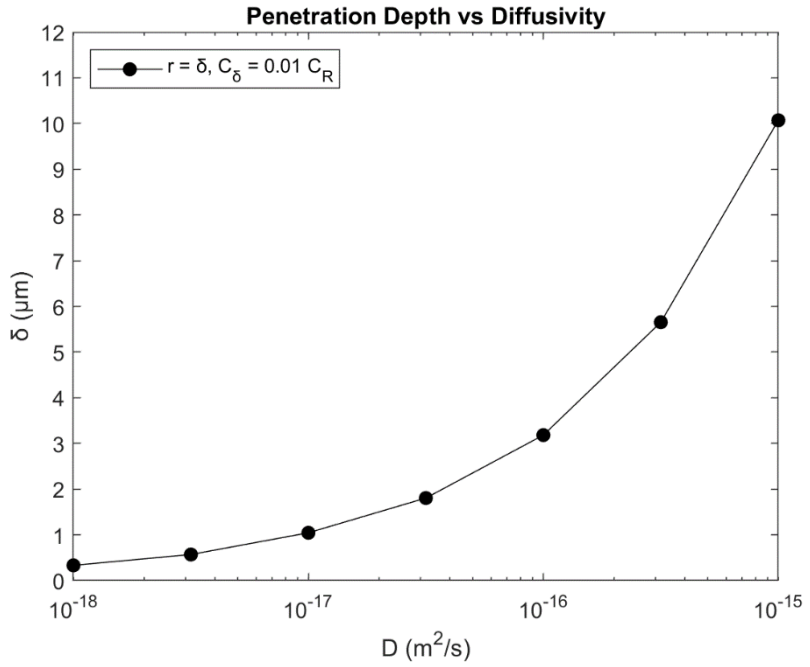

Figure 4.11, Numerical correlation between penetration depth and diffusivity (intensified method).

Based on the numerical analysis of the penetration depth, the relation between diffusivity and penetration depth is simulated. By analysing the penetration depth obtained from SEM, with this correlation, the diffusivity of MNP during impregnation is estimated to be approximately $2 \times 10^{-5} \frac{\mu m^2}{s}$ and within this order of magnitude during the impregnation process. During the intensified impregnation process, a small portion of the ferrofluid and PS/DVB leaked into the condenser compartment. This leakage will reduce the accuracy of the established connection between the numerical correlation and the obtained SEM result from that process.

The numerically calculated diffusivity is compared with simulation results of molecular dynamic models for nanoparticle (NP) diffusion based on the hopping mechanism in irreversibly cross-linked polymers [49], [50].

According to their approach [49], for large-size NP diffusion in cross-linked polymeric networks, the constrain release mechanism [53] characterised by the release of entanglements is not the mode of diffusion. In contrast, the hopping of NP initiated by fluctuations of the polymeric network consisting of entanglement and cross-links acting as strands in the polymer network are responsible for the diffusion of NP.

Their results show that NP dynamics depend on a confinement parameter [51]. This parameter is the ratio of the NP diameter (σ_N) to the dynamic localization length of the cross-links (λ), as it is given in Equation (4-1) [49], [51]. Accordingly, the dynamical regime of NP is categorized into weak, strong, and extreme confinement.

$$C = \frac{\sigma_N}{\lambda} \tag{4-1}$$

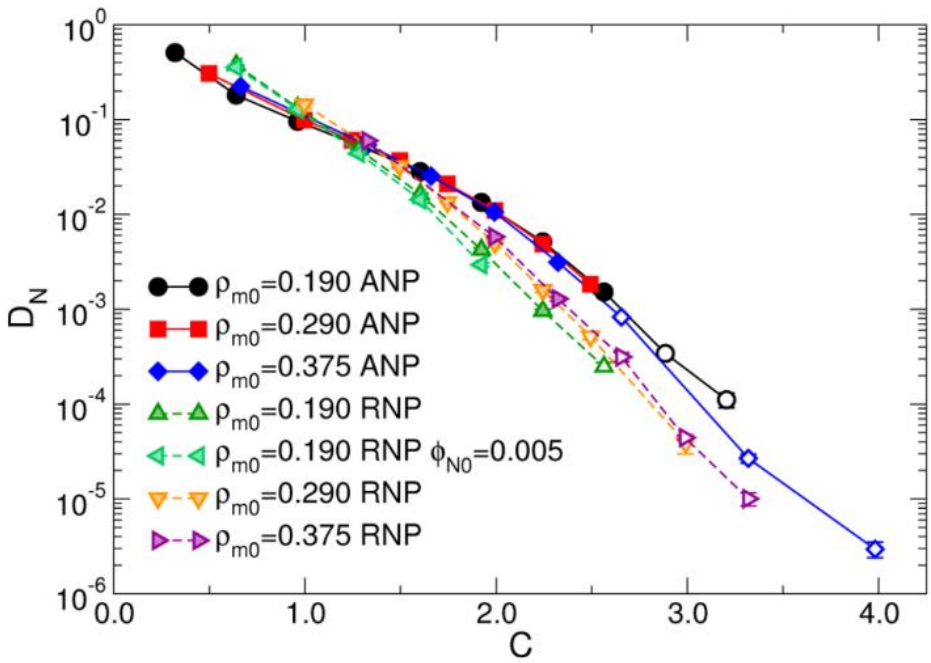

Figure 4.12, Molecular dynamics of NP diffusion at various cross-link densities (ρ_{m_0}) of a cross-linked disordered and polydisperse network [49]. Unless stated, NP volume fraction ($\emptyset_{N0}$) equals to 0.02. ANP and RNP both refer to attractive and repulsive nanoparticles.

The confinement parameter is obtained from the result generated by the molecular dynamics model to evaluate the numerically obtained diffusivity. Accordingly, the diffusion of MNP particles in the cross-linked PS/DVB polymeric network is characterised by a confinement parameter of approximately 3, indicating a strong/extreme confinement regime. In this dynamical regime, NP diffusion is enabled via activated hopping [49].

4.3 Adsorption performance

The impregnation of resins by MNP will compromise its adsorptive capacity to a certain degree. The incorporation of MNP on adsorptive sites renders previously available sites for adsorption unavailable. Pore blocking due to the adsorption of MNP inside the porous structure of the resin is also a contributing factor. This causes capacity reduction since it hinders the accessibility of adsorptive sites. Furthermore, during the impregnation process, swelling and subsequent deswelling of the resins cause changes in the internal crosslink structure. Thus, the capacity is also affected. Therefore, a reduction in the adsorptive capacity of impregnated resins is expected.

4.3.1 Batch adsorption results

The concentrated fermented wastewater stream and the diluted solutions are brought in contact with impregnated and non-impregnated resins inside a flask and left to equilibrate inside the isothermal shaking bath overnight. The detail of this batch experiment examining the adsorptive capacity of relevant compounds is provided in Table 4.3.

Table 4.3, Details of the batch adsorption experiment incorporating artificially made fermented wastewater

Experiment parameters	Value
Mass of liquid (W_l)	10 g
Mass of resin (W_s)	300 mg
Fraction of MNP in impregnated resins (y_{mnp})	0.050
Initial mass fraction of each individual VFA (x_{0_i})	0.0025, 0.0050, 0.0075, 0.0100 0.0125
Mixing rate in the shaking hot bath	120 rpm
Temperature of the shaking-bath	25°C
Batch adsorption duration.	Overnight

By applying the analysis to the solution before and after the experiment and incorporating the correct parameters into Equation (3-1), the relevant isotherms for VFA and phosphoric acids are obtained and graphically shown in Figure 4.13. The IC analysis of samples before and after the batch adsorption experiments shows that chloride, sodium and potassium adsorption did not occur as their concentrations remained the same despite the batch adsorption experiment.

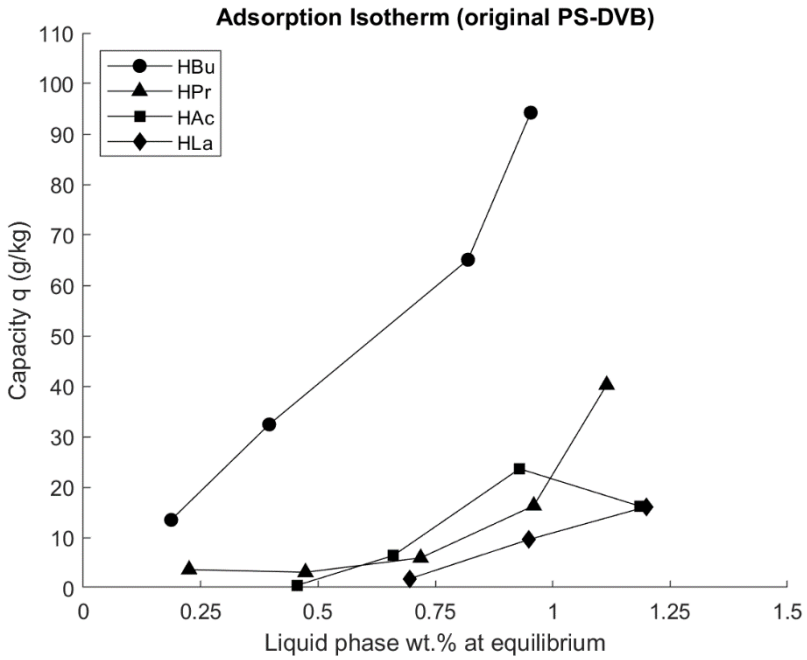

Figure 4.13, Adsorption isotherms of VFA on the original PS/DVB at 25 °C, 1 atm and rpm = 120.

By examining the peaks of each isotherm curve in Figure 4.13 and Figure 4.14, the capacity of impregnated and original resin concerning the species is determined. By comparing the results, the expected decline in adsorptive capacity is noticeable. The capacity of each species on different resins is given in Table 4.4.

Table 4.4, Comparison of VFA and H_3PO_4 adsorption capacity on impregnated and original PS/DVB

Adsorbate	Capacity of PS/DVB (g/kg)	Capacity of impregnated. PS/DVB (intensified) (g/kg)	Difference (%)
HBu	94.2	79.3	- 16%
HPr	40.3	23.8	- 41%
HAc	23.6	17.1	- 27%
HLa	16.1	15.4	- 4.3%
H_3PO_4	17.9	16.9	- 5.6%
Total (VFA)	174.2	135.6	- 22%

The original PS/DVB resins have a total VFA capacity of 174.2 g/kg, whereas the VFA capacity of impregnated resins is compromised by 22% and has reached a total value of 135.6 g/kg. For practical applications, a trade-off between the degree of MNP impregnation and adsorptive capacity should be made in which both heat generation capabilities and the adsorptive capacities of resins are adequate for their purpose.

Phosphoric acid is the only mineral acid observed to be adsorbed on the impregnated and non-impregnated resins. It is only adsorbed when a high phosphoric acid concentration is available in the liquid phase. The corresponding adsorption isotherm is available in Figure 4.15.

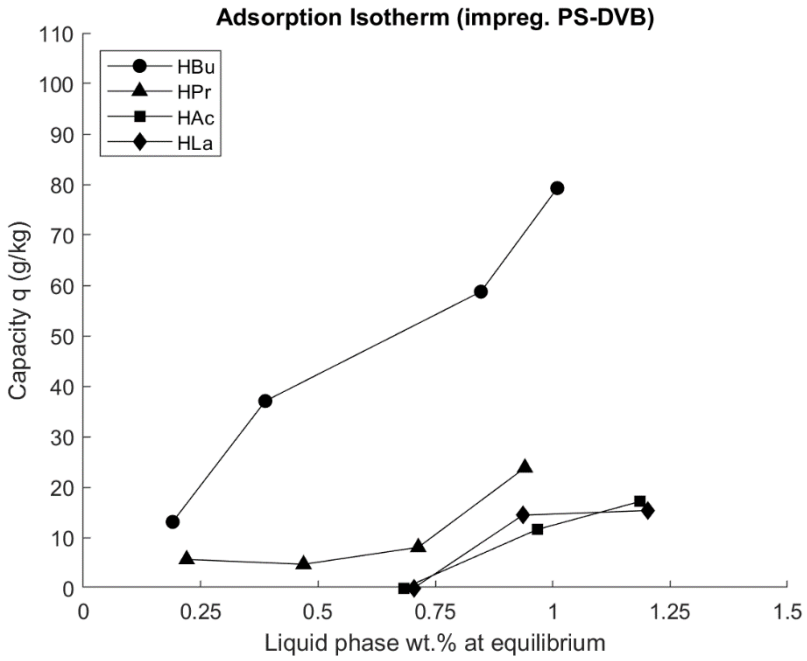

Figure 4.14, Adsorption isotherms of VFA on impregnated PS/DVB at 25 °C, 1 atm and rpm = 120.

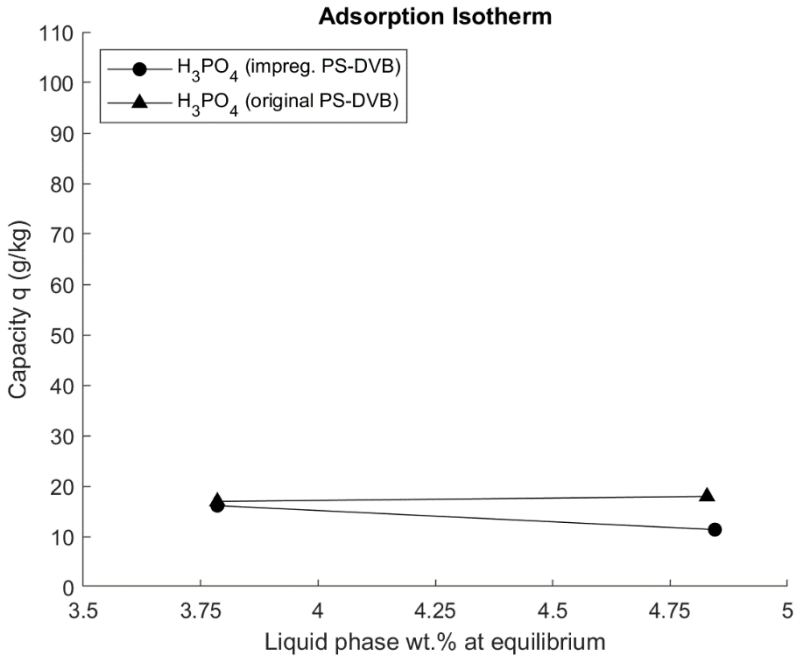

Figure 4.15, Adsorption isotherms of Phosphoric acid on the original PS/DVB at 25 °C, 1 atm and rpm = 120.

4.3.2, ZLC and column adsorption results

Only one ZLC screening experiment with diluted fermented wastewater solutions is carried out. The ZLC experiment is conducted using a column that utilises plungers and holds the resins precisely at the height of less than 8mm. Unfortunately, this column was broken after the first experiment, and a small column with relatively large empty spaces was chosen as a substitute for the ZLC experiment. The data of the screening experiment were collected at a 15-minute interval which is not sufficiently small enough to make diffusivity calculations of the adsorbing compounds. All the compounds reached their final asymptote weight fraction in the liquid phase before the second samples were taken.

The screening ZLC results are obtained by analysing samples taken from the recycle stream in the experimental setup. HPLC results of the obtained samples reveal the following concentration profile given in Figure 4.16 during the ZLC experiment.

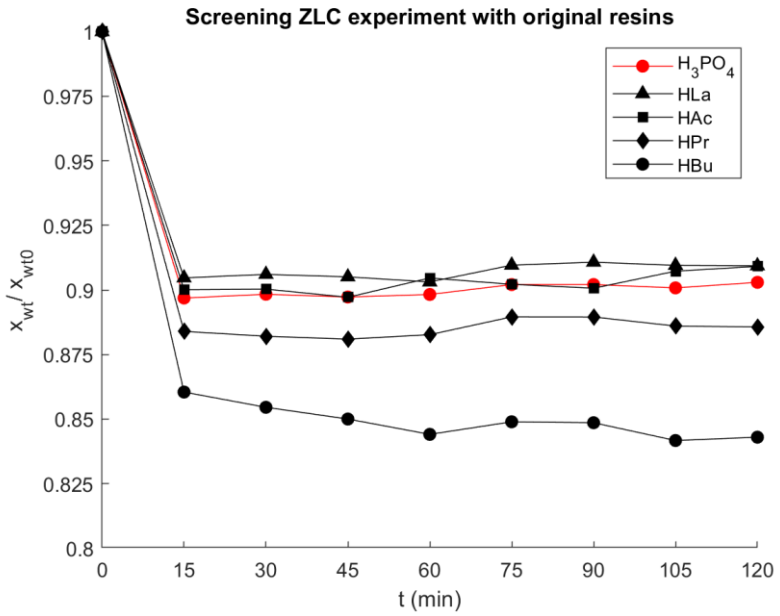

Figure 4.16, ZLC concentration profile, revealing the competitive adsorption of compounds (X_{wt0} = 0.25% for VFA).

In the ZLC experiment, compared to the batch experiment, boundary mass transfer limitations are alleviated by applying a high liquid flow rate through the adsorption column. Thus, adsorption of VFA is expected to occur at a higher capacity, and consequently, the treated liquid phase will have a lower VFA and mineral acid weight fraction. By comparing the result of Figure 4.16 with Figure 4.13, while considering the details of the experiments given in Table 4.5, this experimental setting can surpass the capacity measured in the batch adsorption experiments.

Table 4.5, Details of the screening ZLC experiment.

Detail	Value
Mass of resin	250 mg
Flow rate of liquid	25 ml/min
VFA concentration in liquid phase	0.25%
Mass of the liquid	30 gr
Sampling interval	15 mins
Mixing rate	400 rpm

A comparative second experiment was conducted in a column in which the resins were kept at a minimal height of approximately 8 mm, but on the other hand, this column also contained dead spaces above the fixed zone. Thus, in the second experiment, the effect of axial dispersion is not entirely negligible. Consequently, this resulted in fitting errors when using established methods of calculating diffusivity [44]. The details of the column adsorption experiment are given in Table 4.6. The flow rate of the liquid in this experiment is reduced to perceive better the transition of concentration over time in smaller time intervals.

Table 4.6, Details of the column adsorption experiment.

Detail	Value
Mass of resin	750 mg
Flow rate of liquid	8 ml/min
VFA concentration in liquid phase	0.25%
Mass of the liquid	75 gr
Sampling interval	5 minutes
Total run	2 hrs
Mixing rate	400 rpm

In this experiment, due to axial dispersion effects, the concentration of phosphoric acid, acetic acid and lactic acid after the adsorption column demonstrated a chaotic behaviour in which oscillatory desorption and subsequent adsorption follow initial adsorption. On the other hand, the concentration of butyric acid and propionic acid demonstrates a steady decline over time. Furthermore, the impregnated resins demonstrate a higher selectivity in adsorbing VFA than mineral acids.

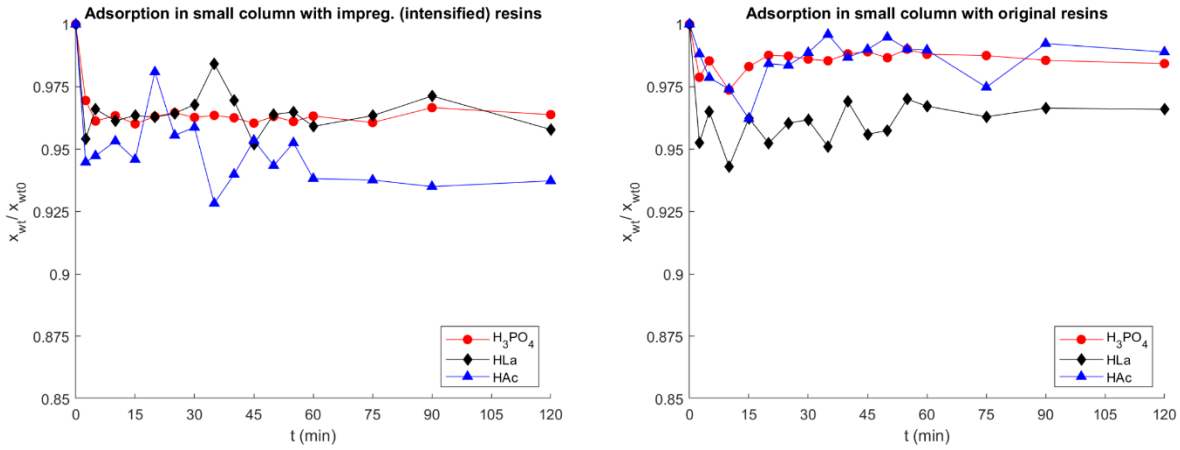

Figure 4.17, Oscillatory & random behaviour due to axial dispersion effects.

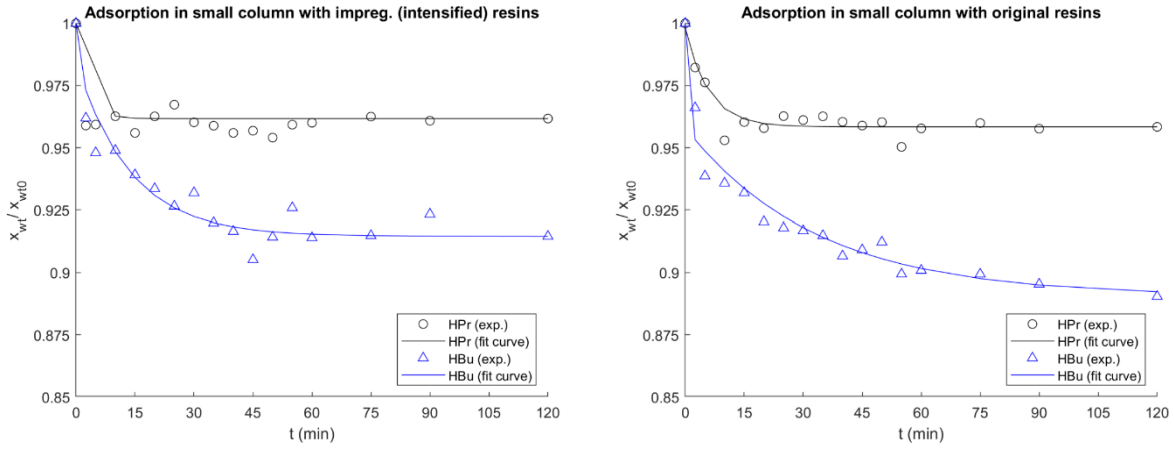

Figure 4.18, Steady decline of butyric and propionic acid throughout the small bed adsorption experiment.

Table 4.7, Diffusivity of compounds with a steady decline obtained from small bed adsorption experiment.

Adsorbate	Diffusivity (m^2/s)
HPr	2×10^{-9}
HBu	4×10^{-10}

The concentration decline of butyric acid and propionic acid in the liquid phase during the small bed adsorption experiment is not significantly dependent on the MNP coating layer. The differences are within the margin of error. The diffusivity of both compounds in both instances is similar and in the same order of magnitude.

4.4 Hyperthermia performance

The application of MNP impregnated resins as a heat source in desorption processes relevant to the treatment of fermented wastewater is investigated. The heat generation per mass of MNP is measured through a hyperthermia experiment.

As discussed in the previous sections, a hyperthermia experiment is conducted using samples inside an insulated cylindrical tube under the influence of AMF. The upper part of the tube is open to enable access of a thermal probe into the column holding the sample.

The experiment is conducted on five different samples and a blank case only containing ethanol. Three samples of this experiment are mixtures of a liquid phase and coated MNP, and the other two are a mixture of ethanol and resins impregnated at normal or intensified conditions. By initiating the AMF by the solenoid, the following temperature profiles are recorded and visually shown in Figure 4.19.

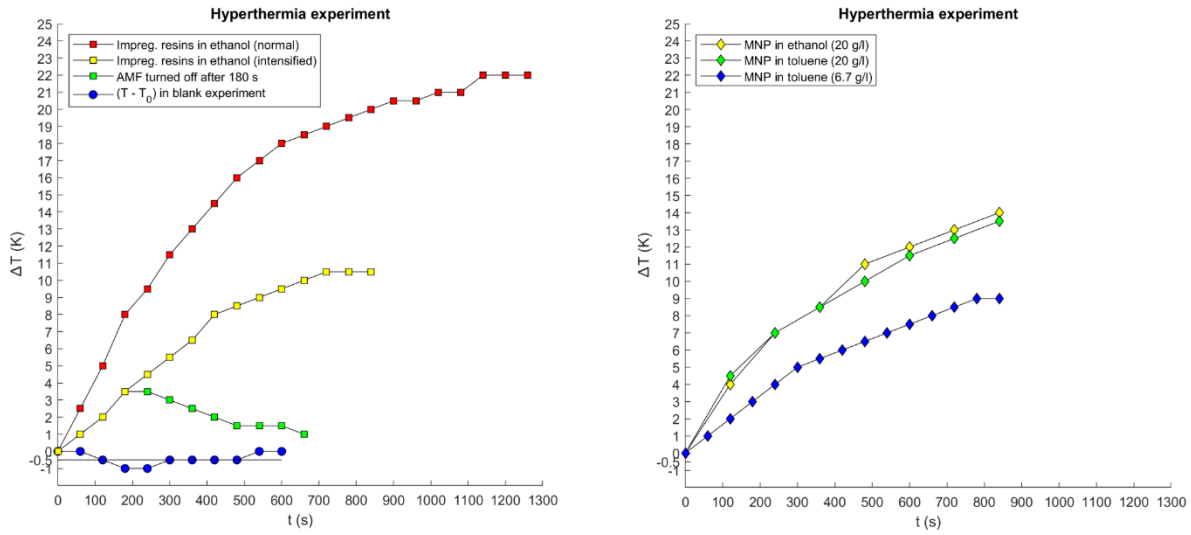

Figure 4.19, Temperature profile of different samples over the course of hyperthermia experiment.

Based on the temperature profile and the specific heat of the mixtures at constant pressure, SAR is measured at the initial condition according to the simplified energy balance form, Equation (3-2). One of the underlying assumptions in obtaining Equation (2-2) from the simplified version is the temperature uniformity between the solid and liquid phases. This assumption is valid since the temperature changes in the transient experiment after the AMF is turned off are approximately close to the standard deviation of the blank experiment. Thus, the significance of the temperature difference between the solid and liquid phases is unimportant.

The SAR is calculated based on the mixture composite in Table 4.8. To compare its heat generation efficiency, the SAR is converted from a kg of mixture basis to kg of MNP basis in Table 4.9. Comparing the values obtained within the possible margin of error makes it apparent that the MNP has retained its superparamagnetic characteristics in all instances.

Table 4.8, The hyperthermia on the mass basis of the mixture.

Case	Specific constant pressure heat of mixture (J/Kg K)	Initial slope of temperature (K/s)	SAR based on mixture (W/ Kg)
MNP in toluene (20 g/l)	1474	0.0375 ± 0.0066	55 ± 10
MNP in toluene (6.7 g/l)	1474	0.0167 ± 0.0066	25 ± 10
MNP in ethanol (20 g/l)	2620	0.0333 ± 0.0066	87 ± 17
Impregnated resins (intensified) in ethanol	2062	0.0167 ± 0.0066	34 ± 14
Impregnated resins (normal) in ethanol	2062	0.0417 ± 0.0066	86 ± 14

Table 4.9, The hyperthermia on the mass basis of the MNP.

Case	Concentration of MNP (g/l)	Density of mixture (kg/l)	SAR based on MNP (kW/kg)
MNP in toluene (20 g/l)	20.0	0.864	2.4 ± 0.4
MNP in toluene (6.7 g/l)	6.7	0.864	3.2 ± 1.3
MNP in ethanol (20 g/l)	20.0	0.798	3.5 ± 0.7
Impregnated resins (intensified) in ethanol	9.2	0.863	3.2 ± 1.3
Impregnated resins (normal) in ethanol	28.2	0.863	2.6 ± 0.4

The impregnated resins via the normal condition demonstrate a higher heat generation density than the impregnated resins via the intensified method, and their MNP content is three times higher than the alternative. Nevertheless, impregnated resins via both methods show relatively similar heat generation per one kg of MNP. Thus, the extent of impregnation does not affect the efficiency of the MNP in generating heat under AMF.

The SAR calculated on both bases (Mass of mixture and mass of MNP) also depends on the characteristics of the AMF. Therefore, it is possible to further increase the heat generation via this method by applying an AMF with a higher frequency and amplitude.

Chapter 5: Conclusion & prospective

5.1 Conclusion

The rationale for applying the impregnation process was to embed magnetite nanoparticles at the core of the PS/DVB resins. The method was developed as an alternative to the suspension polymerisation process in which MNP is added during the polymerisation reaction of PS monomers [7], [8].

According to the SEM analysis, enmeshment of MNP and PS/DVB with full coverage on the external surface of PS/DVB beads impregnated via the intensified method was achieved. Previously, similar core/shell composite materials have been synthesised [54]–[56]. But in these cases, the polymeric structure was polystyrene microspheres (radius < 1 μm) without any crosslinks.

Nevertheless, even though the impregnation of PS/DVB at the intensified method only has a penetration depth of approximately 1.5 μm, it demonstrates heat generation capabilities under AMF and adsorption capacities promising for implementation in a desorption column in the downstream section of a wastewater treatment plant.

A typical desorption column contains tonnes of adsorptive beads. Thus, heat generation through this approach can reach scales of MW output when an AMF influences them with a high amplitude close to 300 mT and frequency in the range of MHz. This innovative heating route via AMF allows for the direct conversion of electricity to heat. Thus, it enables electrification of the adsorption columns, which is one of the ways to decarbonize this chemical industry [57]. Furthermore, heat generated on the surface of the adsorptive beads facilitates a better heating mechanism as convective heat transfer resistance at the gas/solid interfacial layer is alleviated since it operates as a generative heat layer under AMF. Moreover, since the heat generation occurs on the beads' external layer, it may improve desorption under vacuum conditions as secondary adsorption of desorbed compounds on the surface of beads is curtailed.

Furthermore, the measured VFA adsorption capacity of the impregnated resins is on par with commonly applied adsorptive resins for VFA separation. Based on the batch adsorption results, only 22% of VFA adsorption capacity is reduced. According to the ZLC experiment, there was not a significant change in the diffusivity of the adsorbing compounds.

Additionally, this nanocomposite structure enables an alternative separation method of bioproducts using only a simple magnet [21]. Common ways to separate biomass would require ultrafiltration, ultracentrifugation, and micro-dialysis, which are comparatively more costly than applying a simple magnet. Magnetic nanoparticles are also suitable sites for immobilising enzymes facilitating metabolic reactions [58], [59]. Magnetic nanoparticles without a substrate are small sized to act as a support, and they lack the necessary mechanical stability. The impregnated resins with immobilised enzymes on top of the diffusion layer enable a simple separation mechanism and enhance the stability and reusability of enzymes utilised in bioreactors [58].

The experiments conducted in this report demonstrate a proof of concept that impregnated resins via the intensified method are adsorptive mediums enabling hyperthermia heating mechanisms in desorption columns. These speciality resins displayed high selectivity toward VFA in a mineral-rich environment despite its addition of MNP content due to impregnation. In addition, the produced material can provide additional functionalities such as enabling a facile bioseparation mechanism and enzyme immobilisation.

5.2 Prospective

Commercialising the impregnated resins at a larger scale necessitates the need to scale up and improve the MNP synthesis or incorporate currently available swell-inducing ferrofluids in the market. The latter approach seems promising but introduces additional obstacles since most currently available ferrofluids are mixtures of organic compounds that may not show azeotropic evaporation. Thus, the solvent will not constantly evaporate throughout the impregnation and will demonstrate violent phase changes during the process, which will hinder the diffusivity of MNP toward the PS/DVB matrix. Nevertheless, it is possible to improve the MNP synthesis and coating by increasing the surface area of the reaction between the liquid phase and the precipitating agent and by applying a filtration stage after the coated MNP synthesis to obtain a uniform small sized product. These approaches can enhance the quality of the synthesised MNP and reduce agglomerates. Thus, improving the economics of the process and increasing the likelihood of a feasible scaled-up pilot plant for the impregnation process. A study on the mentioned parameters and other synthesis parameters given in subsection 2.1.1 is worthwhile.

Furthermore, applying a better heating mechanism can potentially improve the impregnation process. Our approach introduces the vacuum rotary evaporator heating through a liquid heating bath at a fixed temperature of 80°C. Increasing the impregnation temperature and further reducing the vacuum pressure may be beneficial to allow a better diffusion mechanism. Nevertheless, in this case, the volatility of the MNP surfactant and the ferrofluid solvent must be considered. Compared to this research, operation under more extreme circumstances may necessitate incorporating a different solvent and surfactant.

Nevertheless, in a scaled-up impregnation process, concerns regarding pressure control and inhomogeneity of flow regimes and mixings must be addressed [60]. Furthermore, it may also be of interest to look deeper into the capillary impregnation part of the impregnation process besides the diffusional part by using a molecular dynamic model which considers the interaction of MNP with the PS/DVB resins at the interface during the impregnation. Such a model is potentially beneficial in optimising the process by reducing the amount of required solvent.

Although researching ways to improve the production of impregnated resins is beneficial for scale-up, studies on the implementation of large AMF to enable hyperthermia in a desorption system utilising the impregnated resins are also critical. The most basic AMF delivery solution is a large solenoid wrapping around the desorption column. In this conceptual design, such a device's energy demand and loss must be measured and compared with the energy output via hyperthermia inside the column. Furthermore, heat dissipation through the coils conducting a high electric current poses a significant obstacle and requires additional heat integration [61]. In a future study, capital and operational expenditure comparison with the traditional methods should be investigated once an optimised operating configuration with maximum heat integration is designed.

The results of this research incorporating SEM analysis to measure a diffusion layer would benefit from developing a measuring algorithm that can translate the contrast on SEM images into an average diffusion layer depth. This algorithm will increase the accuracy of the calculated diffusivity of MNP. The diffusivity of MNP forms the basis of calculation for a scale-up version of the impregnation process and hence improving the measurement of this parameter improves the design of a pilot plant.

In this study, the hopping theory has been a reliable way of elucidating NP diffusion. It would be of great interest to produce molecular dynamic models based on this theory. A suitable setting for validating the basis of this theory will examine the effect of physical vibration or sonification with changes in NP concentration inside a polymeric matrix.

In a future study, it may also be of interest to conduct a ZLC experiment with an online measuring instrument to investigate the effect of resin impregnation on the adsorption rate of the rapidly diffusing adsorbates. Compared to the ZLC experiment in this research, this future study will take samples in intervals of a few seconds and is, therefore, able to introduce fewer fittings' errors to the results. Similarly, the impregnation process can also use an online vacuum pressure measuring system inside the flask where diffusion occurs. In this research, the general pressure of the flask in combination with the condenser and the distillate were measured. A local measuring device will make the control scheme and thus the evaporation rate more sensitive and accurate.

By implementing the mentioned theoretical and experimental studies, the path of deciphering the process and its underlying premises will become more lucid.

Reference list:

[1] J. Brusselaers and A. Van Der Linden, 'Bio-waste in Europe—turning challenges into opportunities', 2020, doi: 10.2/JQUERY.MIN.JS.

[2] D. Zhang *et al.*, 'A review: factors affecting excess sludge anaerobic digestion for volatile fatty acids production', *Water Science and Technology*, vol. 72, no. 5, pp. 678–688, 2015, doi: 10.2166/WST.2015.280.

[3] M. Carvalheira and A. F. Duque, 'From Food Waste to Volatile Fatty Acids towards a Circular Economy', *Fermentation-Processes, Benefits and Risks*, 2021, doi: 10.5772/INTECHOPEN.96542.

[4] E. A. Tampio, L. Blasco, M. M. Vainio, M. M. Kahala, and S. E. Rasi, 'Volatile fatty acids (VFAs) and methane from food waste and cow slurry: comparison of biogas and VFA fermentation processes', *Gcb Bioenergy*, vol. 11, no. 1, pp. 72–84, 2019, doi: 10.1111/GCBB.12556/FORMAT/PDF.

[5] E. Reyhanitash, S. R. Kersten, and B. Schuur, 'Recovery of volatile fatty acids from fermented wastewater by adsorption', *ACS sustainable chemistry & engineering*, vol. 5, no. 10, pp. 9176–9184, 2017.

[6] M. Sugiyama, 'Climate change mitigation and electrification', *Energy policy*, vol. 44, pp. 464–468, 2012.

[7] T. Hasell *et al.*, 'Preparation of polymer–nanoparticle composite beads by a nanoparticle-stabilised suspension polymerisation', *Journal of Materials Chemistry*, vol. 17, no. 41, pp. 4382–4386, 2007.

[8] W. Zheng, F. Gao, and H. Gu, 'Magnetic polymer nanospheres with high and uniform magnetite content', *Journal of magnetism and magnetic materials*, vol. 288, pp. 403–410, 2005.

[9] A. Lekhal, B. J. Glasser, and J. G. Khinast, 'Impact of drying on the catalyst profile in supported impregnation catalysts', *Chemical engineering science*, vol. 56, no. 15, pp. 4473–4487, 2001.

[10] M. O. Ruiz, J. L. Cabezas, I. Escudero, and J. Coca, 'Valeric acid extraction with tri-N-butyl phosphate impregnated in a macroporous resin. I. Equilibrium and mass transfer rates', *Separation science and technology*, vol. 39, no. 1, pp. 77–95, 2005, doi: 10.1081/SS-120027402.

[11] Q. Zhang, Y. Han, W.-C. Wang, L. Zhang, and J. Chang, 'Preparation of fluorescent polystyrene microspheres by gradual solvent evaporation method', *European polymer journal*, vol. 45, no. 2, pp. 550–556, 2009.

[12] B. Burghoff, E. Zondervan, and A. B. de Haan, 'Phenol extraction with Cyanex 923: Kinetics of the solvent impregnated resin application', *Reactive and Functional Polymers*, vol. 69, no. 4, pp. 264–271, 2009.

[13] R.-S. Juang and H.-L. Chang, 'Distribution equilibrium of citric acid between aqueous solutions and tri-n-octylamine-impregnated macroporous resins', *Industrial & engineering chemistry research*, vol. 34, no. 4, pp. 1294–1301, 1995.

[14] M. Iqbal and D. Datta, 'Competitive removal of malachite green and Rhodamine-B using Amberlite-XAD-4 impregnated with Aliquat 336: experimental and modelling studies', *Separation Science and Technology*, vol. 55, no. 3, pp. 537–553, 2020.

[15] K. Babić, L. van der Ham, and A. de Haan, 'Recovery of benzaldehyde from aqueous streams using extractant impregnated resins', *Reactive and Functional Polymers*, vol. 66, no. 12, pp. 1494–1505, 2006.

[16] D. N. Muraviev and E. Högfeldt, 'Stability and ion exchange properties of Amberlite XAD-2 impregnated with dinonylnaphthalene sulfonic acid', *Reactive Polymers, Ion Exchangers, Sorbents*, vol. 8, no. 1, pp. 97–102, 1988.

[17] T. Behnke, C. Würth, K. Hoffmann, M. Hübner, U. Panne, and U. Resch-Genger, 'Encapsulation of hydrophobic dyes in polystyrene micro-and nanoparticles via swelling procedures', *Journal of fluorescence*, vol. 21, no. 3, pp. 937–944, 2011.

[18] A. Jordan, P. Wust, H. Fähling, W. John, A. Hinz, and R. Felix, 'Inductive heating of ferrimagnetic particles and magnetic fluids: physical evaluation of their potential for hyperthermia', *International journal of hyperthermia*, vol. 9, no. 1, pp. 51–68, 1993.

[19] R. Hergt *et al.*, 'Physical limits of hyperthermia using magnetite fine particles', *IEEE Transactions on magnetics*, vol. 34, no. 5, pp. 3745–3754, 1998.
[20] S. Brulé *et al.*, 'Doxorubicin release triggered by alginate embedded magnetic nanoheaters: a combined therapy', *Advanced Materials*, vol. 23, no. 6, pp. 787–790, 2011.
[21] A.-G. Niculescu, C. Chircov, and A. M. Grumezescu, 'Magnetite nanoparticles: synthesis methods–a comparative review', *Methods*, 2021.
[22] W. Wu, Z. Wu, T. Yu, C. Jiang, and W.-S. Kim, 'Recent progress on magnetic iron oxide nanoparticles: synthesis, surface functional strategies and biomedical applications', *Science and technology of advanced materials*, 2015, doi: 10.1088/1468-6996/16/2/023501.
[23] L. S. Ganapathe, M. A. Mohamed, R. Mohamad Yunus, and D. D. Berhanuddin, 'Magnetite (Fe3O4) nanoparticles in biomedical application: from synthesis to surface functionalisation', *Magnetochemistry*, vol. 6, no. 4, p. 68, 2020.
[24] D. Thapa, V. R. Palkar, M. B. Kurup, and S. K. Malik, 'Properties of magnetite nanoparticles synthesized through a novel chemical route', *Materials Letters*, vol. 58, no. 21, pp. 2692–2694, 2004.
[25] L. Blaney, 'Magnetite (Fe3O4): Properties, synthesis, and applications', 2007.
[26] S. Liu, B. Yu, S. Wang, Y. Shen, and H. Cong, 'Preparation, surface functionalization and application of Fe3O4 magnetic nanoparticles', *Advances in colloid and Interface Science*, vol. 281, p. 102165, 2020.
[27] K. Petcharoen and A. Sirivat, 'Synthesis and characterization of magnetite nanoparticles via the chemical co-precipitation method', *Materials Science and Engineering: B*, vol. 177, no. 5, pp. 421–427, 2012, doi: 10.1016/J.MSEB.2012.01.003.
[28] G. Gnanaprakash, S. Mahadevan, T. Jayakumar, P. Kalyanasundaram, J. Philip, and B. Raj, 'Effect of initial pH and temperature of iron salt solutions on formation of magnetite nanoparticles', *Materials chemistry and Physics*, vol. 103, no. 1, pp. 168–175, 2007, doi: 10.1016/J.MATCHEMPHYS.2007.02.011.
[29] M. Mahdavi *et al.*, 'Synthesis, surface modification and characterisation of biocompatible magnetic iron oxide nanoparticles for biomedical applications', *Molecules*, vol. 18, no. 7, pp. 7533–7548, 2013.
[30] M. I. Shliomis, A. F. Pshenichnikov, K. I. Morozov, and I. Y. Shurubor, 'Magnetic properties of ferrocolloids', *Journal of magnetism and magnetic materials*, vol. 85, no. 1–3, pp. 40–46, 1990.
[31] W. J. Atkinson, I. A. Brezovich, and D. P. Chakraborty, 'Usable frequencies in hyperthermia with thermal seeds', *IEEE Transactions on Biomedical Engineering*, no. 1, pp. 70–75, 1984.
[32] C. Taddei *et al.*, 'Fabrication of polystyrene-encapsulated magnetic iron oxide nanoparticles via batch and microfluidic-assisted production', *Colloid and Polymer Science*, vol. 297, no. 6, pp. 861–870, 2019, doi: 10.1007/S00396-019-04496-4/FIGURES/12.
[33] X. Liu, M. D. Kaminski, Y. Guan, H. Chen, H. Liu, and A. J. Rosengart, 'Preparation and characterization of hydrophobic superparamagnetic magnetite gel', *Journal of magnetism and magnetic materials*, vol. 306, no. 2, pp. 248–253, 2006.
[34] M. J. Farrall and J. M. Frechet, 'Bromination and lithiation: two important steps in the functionalization of polystyrene resins', *The Journal of Organic Chemistry*, vol. 41, no. 24, pp. 3877–3882, 1976.
[35] S.-H. Kim, Y. Huang, C. Sawatdeenarunat, S. Sung, and V. S.-Y. Lin, 'Selective sequestration of carboxylic acids from biomass fermentation by surface-functionalized mesoporous silica nanoparticles', *Journal of Materials Chemistry*, vol. 21, no. 32, pp. 12103–12109, 2011, doi: 10.1039/C1JM11299F.
[36] S. Rebecchi, D. Pinelli, L. Bertin, F. Zama, F. Fava, and D. Frascari, 'Volatile fatty acids recovery from the effluent of an acidogenic digestion process fed with grape pomace by adsorption on ion exchange resins', *Chemical Engineering Journal*, vol. 306, pp. 629–639, 2016, doi: 10.1016/J.CEJ.2016.07.101.
[37] A. H. da Silva and E. A. Miranda, 'Adsorption/desorption of organic acids onto different adsorbents for their recovery from fermentation broths', *Journal of Chemical & engineering data*, vol. 58, no. 6, pp. 1454–1463, 2013, doi: 10.1021/je3008759.
[38] J. Bokhove, 'Solvent impregnated resins for selective cyanopyridine trace recovery from aqueous streams', 2013, doi: 10.6100/IR760958.

[39] B. H. Hameed and M. I. El-Khaiary, ‘Batch removal of malachite green from aqueous solutions by adsorption on oil palm trunk fibre: equilibrium isotherms and kinetic studies’, *Journal of hazardous materials*, vol. 154, no. 1–3, pp. 237–244, 2008.
[40] A. Mittal, L. Krishnan, and V. K. Gupta, ‘Removal and recovery of malachite green from wastewater using an agricultural waste material, de-oiled soya’, *Separation and Purification Technology*, vol. 43, no. 2, pp. 125–133, 2005.
[41] J. D. Seader, E. J. Henley, and D. K. Roper, *Separation process principles: With applications using process simulators*. John Wiley & Sons, 2016.
[42] N. Schouten, L. G. van der Ham, G.-J. W. Euverink, and A. B. de Haan, ‘Kinetic analysis of anionic surfactant adsorption from aqueous solution onto activated carbon and layered double hydroxide with the zero length column method’, *Separation and purification technology*, vol. 68, no. 2, pp. 199–207, 2009.
[43] S. Corderí, C. R. Vitasari, M. Gramblicka, T. Giard, and B. Schuur, ‘Chiral separation of naproxen with immobilized liquid phases’, *Organic process research & development*, vol. 20, no. 2, pp. 297–305, 2016.
[44] S. Brandani, J. Hufton, and D. Ruthven, ‘Self-diffusion of propane and propylene in 5A and 13X zeolite crystals studied by the tracer ZLC method’, *Zeolites*, vol. 15, no. 7, pp. 624–631, 1995.
[45] J. Dunnewijk, H. Bosch, and A. B. de Haan, ‘Adsorption kinetics of CoCl2 and PPh3 over macroreticular and gel type adsorbents by a generalized ZLC method’, *Chemical engineering science*, vol. 61, no. 15, pp. 4813–4826, 2006.
[46] J. Crank and E. P. J. Crank, *The Mathematics of Diffusion*. Clarendon Press, 1979. [Online]. Available: https://books.google.nl/books?id=eHANhZwVouYC
[47] F. Yan *et al.*, ‘Synthesis and characterization of silica-embedded iron oxide nanoparticles for magnetic resonance imaging’, *Journal of Nanoscience and Nanotechnology*, vol. 4, no. 1–2, pp. 72–76, 2004.
[48] M. Song, W. K. Moon, Y. Kim, D. Lim, I.-C. Song, and B.-W. Yoon, ‘Labeling efficacy of superparamagnetic iron oxide nanoparticles to human neural stem cells: comparison of ferumoxides, monocrystalline iron oxide, cross-linked iron oxide (CLIO)-NH2 and tat-CLIO’, *Korean Journal of Radiology*, vol. 8, no. 5, pp. 365–371, 2007.
[49] V. Sorichetti, V. Hugouvieux, and W. Kob, ‘Dynamics of nanoparticles in polydisperse polymer networks: From free diffusion to hopping’, *Macromolecules*, vol. 54, no. 18, pp. 8575–8589, 2021.
[50] L.-H. Cai, S. Panyukov, and M. Rubinstein, ‘Hopping diffusion of nanoparticles in polymer matrices’, *Macromolecules*, vol. 48, no. 3, pp. 847–862, 2015.
[51] Z. E. Dell and K. S. Schweizer, ‘Theory of localization and activated hopping of nanoparticles in cross-linked networks and entangled polymer melts’, *Macromolecules*, vol. 47, no. 1, pp. 405–414, 2014.
[52] V. G. Geethamma, R. Asaletha, N. Kalarikkal, and S. Thomas, ‘Vibration and sound damping in polymers’, *Resonance*, vol. 19, no. 9, pp. 821–833, 2014.
[53] U. Yamamoto and K. S. Schweizer, ‘Microscopic theory of the long-time diffusivity and intermediate-time anomalous transport of a nanoparticle in polymer melts’, *Macromolecules*, vol. 48, no. 1, pp. 152–163, 2015.
[54] Z. Huang and F. Tang, ‘Preparation, structure, and magnetic properties of polystyrene coated by Fe3O4 nanoparticles’, *Journal of Colloid and Interface Science*, vol. 275, no. 1, pp. 142–147, 2004.
[55] H. S. Chae, S. H. Piao, W. J. Han, and H. J. Choi, ‘Core/shell polystyrene/magnetite hybrid nanoparticles fabricated by pickering emulsion polymerization and their magnetorheological response’, *Macromolecular Chemistry and Physics*, vol. 219, no. 5, p. 1700408, 2018.
[56] Z. Huang, F. Tang, and L. Zhang, ‘Morphology control and texture of Fe3O4 nanoparticle-coated polystyrene microspheres by ethylene glycol in forced hydrolysis reaction’, *Thin Solid Films*, vol. 471, no. 1–2, pp. 105–112, 2005.
[57] Z. J. Schiffer and K. Manthiram, ‘Electrification and decarbonization of the chemical industry’, *Joule*, vol. 1, no. 1, pp. 10–14, 2017.

[58] J. Xu, J. Sun, Y. Wang, J. Sheng, F. Wang, and M. Sun, 'Application of iron magnetic nanoparticles in protein immobilization', *Molecules*, vol. 19, no. 8, pp. 11465–11486, 2014.
[59] X. Meng, G. Xu, Q.-L. Zhou, J.-P. Wu, and L.-R. Yang, 'Highly efficient solvent-free synthesis of 1, 3-diacylglycerols by lipase immobilised on nano-sized magnetite particles', *Food Chemistry*, vol. 143, pp. 319–324, 2014.
[60] M. Campanati, G. Fornasari, and A. Vaccari, 'Fundamentals in the preparation of heterogeneous catalysts', *Catalysis today*, vol. 77, no. 4, pp. 299–314, 2003.
[61] M. G. Christiansen, C. M. Howe, D. C. Bono, D. J. Perreault, and P. Anikeeva, 'Practical methods for generating alternating magnetic fields for biomedical research', *Review of Scientific Instruments*, vol. 88, no. 8, p. 084301, 2017.

Appendix A: Coated MNP synthesis

The synthesis of MNP with the correct size and morphology is crucial for the impregnation of PS/DVB resins. The co-precipitation route is applied in this synthesis. In this manner, first, an acidic medium is created with hydrogen chloride. The mixture is moved into a three-way flask and purged from oxygen using nitrogen flow (low pressures). The container flask has an opening for a mechanical stirrer, nitrogen inflow, and a pressure regulator. The pressure regulator and mechanical stirrer are removed to introduce surfactant compounds or salts during crystallisation. The three-way flask is maintained inside a sonification and heater bath. The configuration of the synthesis setting is shown in Figure A.1.

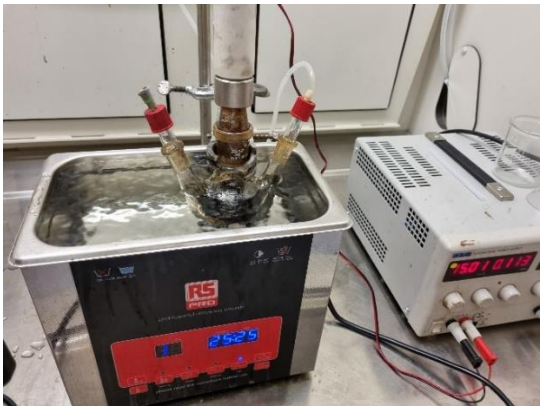

Figure A.1, The three-way flask is kept within the heater and sonification bath.

The synthesis of 2.00 gr of MNP coated with **oleic acid** includes the following chronological steps:

1. A 100 ml acidic aqueous solution with a pH of 2 is produced using hydrogen chloride (>37%) and milli-q water.

2. The solution is transferred to the three-way flask with the proper configuration according to Figure A.1, using a funnel.

3. Oxygen is purged from the three-way flask by using nitrogen flow. During this step, the bath temperature is kept at room temperature (below 20°C) by adding ice to the heating bath. In this step, mechanical mixing and sonification are activated and kept on during the whole process to make the mixture homogenous. This step should prolong for at least 15 minutes.

4. 2.802 ($FeCl_3$) gr of iron (III) chloride and 1.717 gr ($FeCl_2.4H_2O$) of iron (II) chloride tetrahydrate, which represent a molar ratio of 2:1 and corresponds to the formation of 2 gr of MNP at total conversion are introduced into the mixture and stirred for 1 hour at room temperature using ice.

The amount calculated for this step 4 is based on Equation (2-1). The conversions are written below:

$$2\ \text{gr}\ Fe_3O_4\ \text{x}\ \frac{1\ \text{mol}\ Fe_3O_4}{231{,}533\ \text{gr}\ Fe_3O_4}\ \text{x}\ \frac{2\ \text{mol}\ Fe^{3+}}{1\ \text{mol}\ Fe_3O_4}\ \text{x}\ \frac{1\ \text{mol}\ FeCl_3}{1\ \text{mol}\ Fe^{3+}}\ \text{x}\ \frac{162.2\ \text{gr}\ FeCl_3}{1\ \text{mol}\ FeCl_3} = 2.802\ \text{gr}\ FeCl_3$$

$$2\ \text{gr}\ Fe_3O_4\ \text{x}\ \frac{1\ \text{mol}\ Fe_3O_4}{231{,}533\ \text{gr}\ Fe_3O_4}\ \text{x}\ \frac{1\ \text{mol}\ Fe^{2+}}{1\ \text{mol}\ Fe_3O_4}\ \text{x}\ \frac{1\ \text{mol}\ FeCl2.4H2O}{1\ \text{mol}\ Fe^{2+}}\ \text{x}\ \frac{198.75\ FeCl2.4H2O}{1\ \text{mol}\ FeCl2.4H2O} = 1.717\ \text{gr}\ \ FeCl2.4H2O$$

5. By introducing 30 ml ammonium hydroxide (30%) to the mixture solution, precipitation is initiated inside the mixture and the colour of the solution changes from yellow to black. This step is prolonged for 30 minutes. In this step ice is not added to cool the bath.

6. The bath temperature is increased slowly from room temperature to 80°C (approximately: 1 - 1.5°C /minute). The top surface of the bath is covered with tin foils to improve heat isolation. This step should take around 60 – 90 minutes.

7. When the temperature has reached 80°C, 1.2 ml (0.85% of total mixture volume) of surfactant is added to the mixture. This mixture is kept at the current condition for another 45 minutes.

8. The mixture from the three-way flask is removed into beakers where they are mixed with ethanol at three times their initial volume. The beakers are put on top of a strong permanent magnet such as neodymium to facilitate the phaseout of ferrofluids into the bottom of the beakers.

9. While maintaining the permanent magnet outside the beaker and close to the bottom of the beakers, the beakers are phased out from the non-magnetic phase by tilting and releasing the liquid from the top brim of the beaker.

10. The separated ferrofluid is rinsed with 50 ml of ethanol in a sonification bath for 20 minutes.

11. The ferrofluid is dried in a vacuum at 50 °C for 16 hours (overnight) to retrieve magnetite nanoparticles.

The synthesis of 2 gr of MNP coated with **hexanoic acid** includes the following chronological steps:

1. Steps 1-5 from the previous method are followed.

2. Due to the violent reaction of hexanoic acid with alkaline compounds, the liquid from the three-way flask must contain a pH lower than the previous method when this surfactant is added. Therefore, like step 9 in the previous method, the non-magnetic alkaline phase is removed from the three-way flask before heating and adding the surfactant. Furthermore, equal to the amount withdrawn in this step, milli-q water is added.

3. Steps 6-11 from the previous method are proceeded. In step 8, it is not necessary to mix the liquid with ethanol to enhance sedimentation.

Appendix B: Evaporation rate analysis in the rotary evaporator

In this section, the operation of a rotary evaporator is analysed by conducting sensitivity on pressure. The range of operating pressure is varied to investigate its effect on the solvent evaporation rate within the flask. The evaporation rate is calculated by subtracting the initial weight of the flask containing the solvent from its total weight after some time of rotary evaporators' operation. In this analysis, the ferrofluid is represented by pure toluene.

Based on data obtained by the sensitivity analysis, the difference between the operating pressure and the saturation pressure exponentially affects the evaporation rate of the solvent.

Table B.1, Pressure sensitivity analysis on toluene evaporation rate.

Evaporation duration	pressure (/mbar)	Pressure control range	temperature (/°C)	initial weight (/gr)	weight after duration (/gr)	weight of the flask (/gr)	evaporation (/gr)
1 hr	100	(95,110) dp = 10	70	121.05	100.01	99.80	21.04
1 hr	300	(295,310) dp = 10	60	121.38	121.38	99.80	0.00
30 m	330	(325,370) dp = 40	80	121.88	121.58	99.95	0.30
30 m	280	(275,330) dp = 50	80	121.58	121.10	99.95	0.48
30 m	230	(225,280) dp = 50	80	121.10	117.77	99.95	3.33
30 m	240	(235,290) dp = 50	80	113.41	112.25	91.92	1.16
30 m	230	(225,300) dp = 70	80	112.25	111.02	91.92	1.23
30 m	230	(225,290) dp = 60	80	111.02	109.82	91.92	1.20
30 m	220	(215,280) dp = 60	80	109.62	105.99	91.92	3.63
1 hr (50 ml toluene in 100 ml flask)	220	(225, 280) dp = 60	80	169.81	134.00	127.15	35.81
2 hrs	230	(225,290) dp = 60	80	114.69	101.16	93.54	13.53
2 hrs	230	(235,350) dp = 120	80	113.23	111.78	91.80	1.45

Due to the non-linear relationship between the solvent evaporation rate and the difference between the solvent's operating pressure and saturation pressure, it is decided to increase the control range for the dry impregnation. This mode of operation allows periodic evaporation of the solvent when the pressure inside the flask reaches the lower end of the pressure range. Increasing the pressure range inevitably reduces the magnitude of solvent evaporation, which happens more predominantly at the higher pressure control range. Implementing this evaporation approach makes it possible to adjust the evaporation rate more accurately.

According to the result of the sensitivity, operating the rotary evaporator at the conditions given in Table B.2 allows prolonging the intensified impregnation duration for approximately 5 hours.

Table B.2, Feasible operating point for dry impregnation of MNP in a toluene solvent.

Temperature (T)	Pressure (P)	Allowable excessive pressure (dP)	Solvent volume
80 °C	230 mBar	60 mBar	25 ml

A sawtooth waveform is a simplified description of the pressure profile under these operating conditions. The periodic increase of pressure occurs due to toluene evaporation at low-pressure ranges. Furthermore, once the upper limit of pressure is reached, a vacuum pump reduces the pressure to the set value. This profile is graphically shown in Figure B.1.

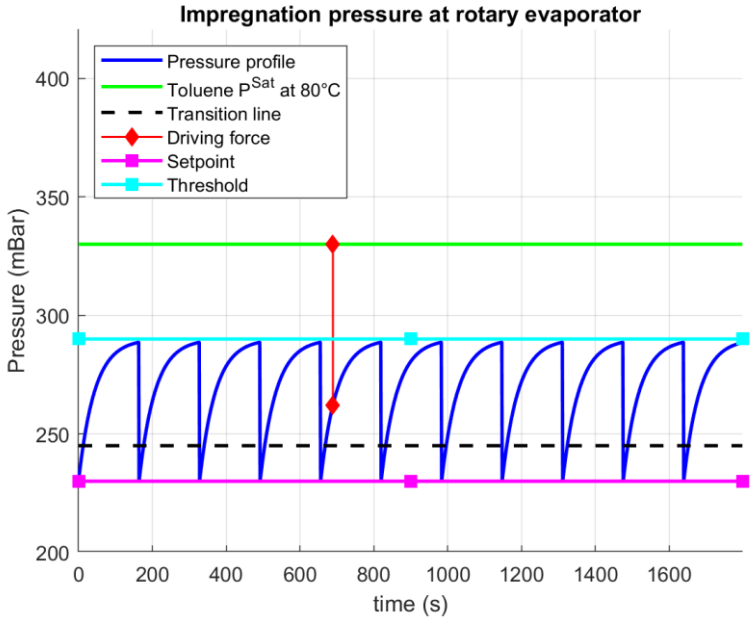

Figure B.1, Pressure profile for slowly evaporating toluene during intensified impregnation.

Appendix C: Amberlite® XAD1180N pre-treatment

Amberlite® XAD1180N resins are pre-treated for impregnation, so their adsorptive capacity is not compromised. The resins are treated with water and nitrogen in adsorption and desorption columns. The laboratory setting for this pre-treatment step is graphically shown in Figure C.1.

Figure C.1, Adsorption desorption column for pre-treatment of PS/DVB.

Initially, the resins are washed in the adsorption column with milli-q water at room temperature and atmospheric pressure. The water flow rate in this adsorption column is 3 ml/min. After two hours of operation, the resins are purged from any water occupying the void area between resins. This is facilitated by using nitrogen flow at room temperature.

The resins washed with water are subsequently moved into the desorption compartment. In this stage, the resins are brought in contact with heated nitrogen at a flow rate of 2.5 l/hour. A feedback control system maintains the temperature of this desorption column at 103 °C. The final element of this heating system is a microwave. The effluent outlet gas stream contains vapour. A condenser retrieves the desorbed water. After two hours of desorption, the total mass of recovered water became constant.

Appendix D: Synthesis of artificially made fermented wastewater

For adsorption experiments, a liquid is artificially synthesised to represent fermented wastewater. According to the composition given in Subsection 3.2.3, this mixture is produced by mixing the four commonplace VFA with three mineral salts. In this scenario, a concentrated solution is initially made, which is subsequently diluted. The volume and mass of each VFA and salt that must be added to synthesise the artificial fermented wastewater is given in Table D.1. For safety reasons, the acids are initially added to 150 ml of the milli-q water. Subsequently, the salts are introduced. Furthermore, after adding all the VFA and salts, the mixture is stirred at 1300 rpm for 3 hours at 30°C.

Table D.1, exact content used to synthesis the artificial fermented wastewater.

Compound name	Amount added (ml or g)	mass fraction (x_k)
HAc	2.17 ml	0.0125
HPr	2.30 ml	0.0125
HBu	2.36 ml	0.0125
HLa	2.2728 g	0.0125
KCl	3.3887 g	0.0186
Na_2SO_4	6.4566 g	0.0355
Na_2HPO_4	12.9060 g	0.0710
milli-q water	150 ml	0.8250
Mixture density	1.2638 g/ml	-
Total mass	181.85 g	-

Table D.2, cation, and anion mass fraction after total dissociation

Ion	mass fraction
Na^+	0.0345
K^+	0.0098
Cl^-	0.0088
SO_4^{2-}	0.0240
PO_4^{3-}	0.0475

Table D.3 explains the dilution factor of the artificially made concentrated version of fermented wastewater. Since most of the ions in this rich mineral liquid have a concentration above 220 ppm, even in the most diluted version, it is necessary to dilute the original or used mixture for a sensible IC measurement. The information regarding the required dilution is given below. On the other hand, HPLC measurement does not require additional dilution of a sample before analysis since the concentration of detectable analytes is already within the sensible range of measurement.

Table D.3, Dilution strategy for experiments and IC measurements.

Individual VFA concentration (wt. %)	Mass of milli-q water added to mass of concentrated version	Required dilution for IC measurement (µl sample in ml milli-q water)
1.25	0 to 30	102 µl in 25 ml
1.00	6 to 24	128 µl in 25 ml
0.75	12 to 18	170 µl in 25 ml
0.50	18 to 12	258 µl in 25 ml
0.25	24 to 6	520 µl in 25 ml

Appendix E: HPLC calibration lines

HPLC is applied to measure the weight percentage of VFA (HLa, HAc, HPr and HBu) and phosphoric acid in aqueous solutions. An artificial fermented wastewater sample is made and diluted with milli-q water according to the approach given in Appendix D To make calibration lines. The diluted samples contain phosphoric acid, and VFA at different weight percentages (0.25%, 0.50%, 0.75%, 1.00% and 1.25% for VFA and 1-5% for phosphoric acid).

The calibration lines correlate the positive integral of a peak of the refractive index (RI) signal detected by HPLC at a specific time window with the weight fraction of a particular analyte in the aqueous phase. The RI peaks sensed at the outlet of the chromatography are distinct to each compound as their retention time to reach the outlet differs according to their affinity with the solid phase. A MATLAB code is produced to create a linear regression of the data using the Poltfit() and Polyval routine. The correlation factor R^2 is also provided along the linearised relation between the area under the peak and the weight fraction of the specific analyte. The operational details and characteristics of the HPLC equipment are given in Table E.1.

Table E.1, Details of the HPLC equipment used for the analysis

Column type	Hi-Plex H (by Agilent)
Pure mobile phase composition	5mM H2SO4
Flow rate of mobile phase	0,6 ml/min
Sample injection into mobile phase	10 µl
Column temperature	65°C
Available detectors	Refractive index detector (RID) Variable wavelength detector (VWD)
Temperature of detectors	55°C
Pressure	30 bar

The calibration lines and their graphical representations with respect to VFA and phosphoric acid are provided in the following pages.

E.1 Phosphoric acid calibration line

Table E.2, HPLC results from the reference mixture samples

Weight percentage of phosphoric acid (wt. %)	Average of area
0.98%	850038.6
1.96%	1719701
2.94%	2619303.3
3.92%	3725595.5
4.90%	4742159

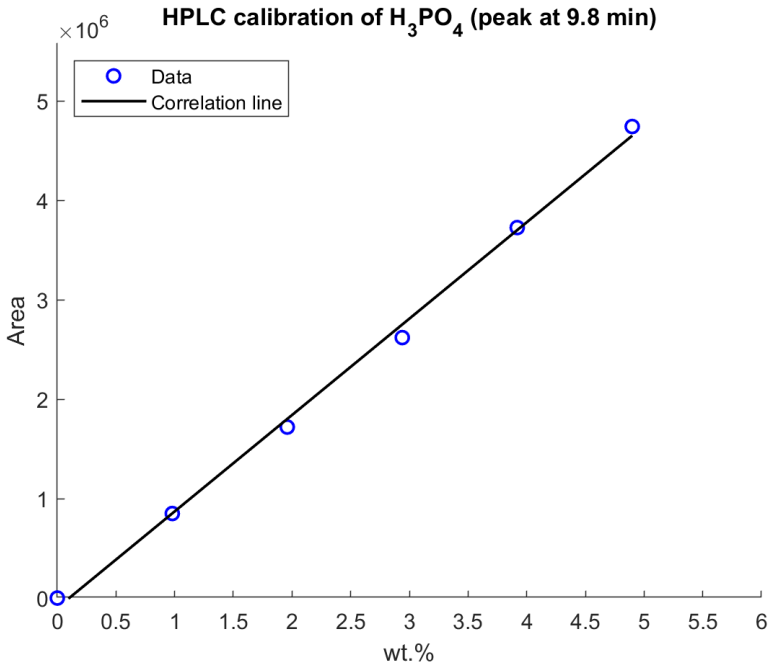

Figure E.1, correlation between phosphoric acid weight percentage and the area under refractive index signal.

$$wt.\,\% = 1.029\ 10^{-8}\ X_{area} - 0.0011 \qquad (R^2 = 0.997) \qquad \text{(E-1)}$$

E.2 Lactic acid calibration line

Table E.3, HPLC results from the reference mixture samples.

Weight percentage of lactic acid (wt. %)	Average of area
0.25%	241673.6
0.50%	476058.3
0.75%	741883.9
1.00%	1034313.4
1.25%	1320226

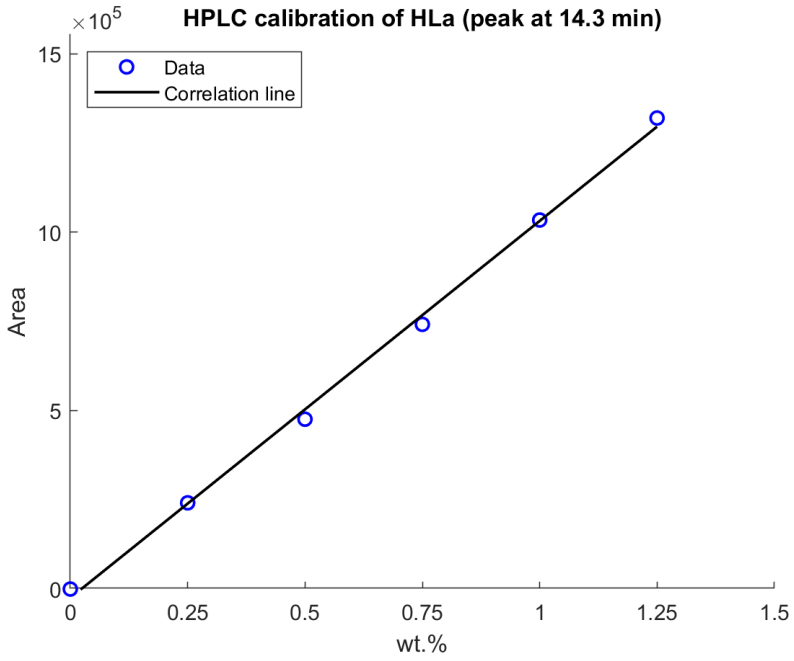

Figure E.2, correlation between lactic acid weight percentage and the area under refractive index signal.

$$wt.\,\% = 9.444\ 10^{-9}\ X_{area} - 0.0002 \qquad (R^2 = 0.998) \qquad \text{(E-2)}$$

E.3 Acetic acid calibration line

Table E.4, HPLC results from the reference mixture samples.

Weight concentration of acetic acid (wt. %)	Average of area
0.25%	155888
0.50%	319598
0.75%	474345.6
1.00%	697718.6
1.25%	861217

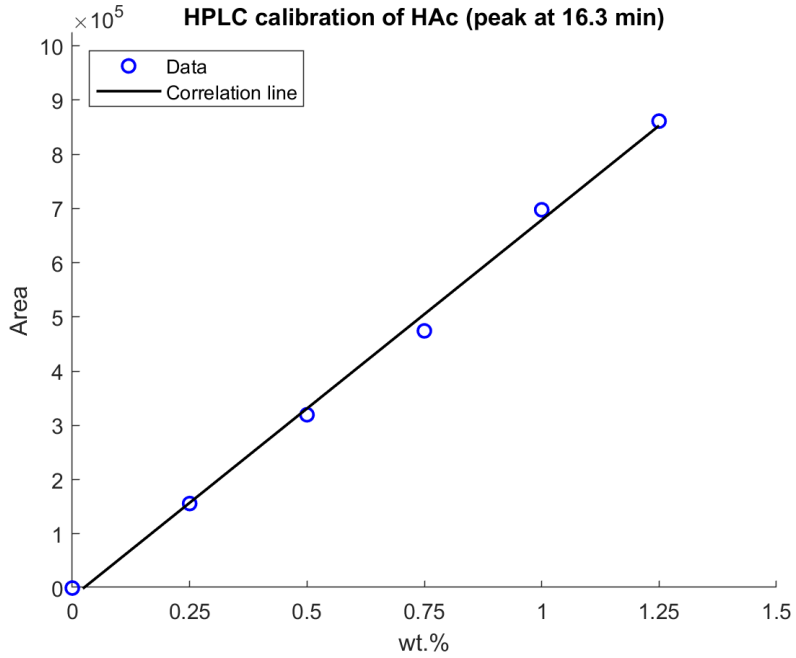

Figure E.3, correlation between lactic acid weight percentage and the area under refractive index signal.

$$wt.\,\% = 1.432\ 10^{-8}\ X_{area} - 0.0002 \qquad (R^2 = 0.996) \tag{E-3}$$

E.4 Propionic acid calibration line

Table E.5, HPLC results from the reference mixture samples.

Weight concentration of acetic acid (wt. %)	Average of area
0.25%	199550.4
0.50%	407446.5
0.75%	621805.2
1.00%	851105.9
1.25%	1042768.9

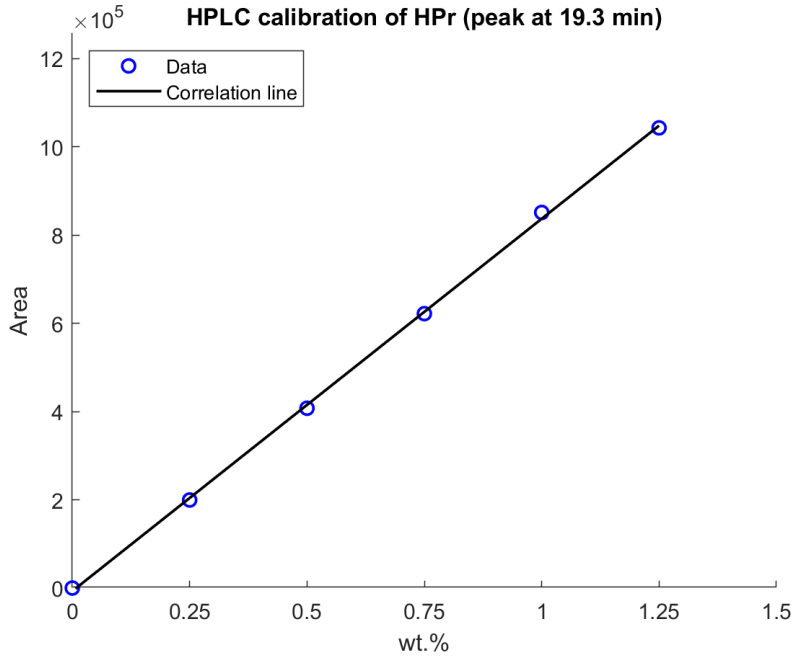

Figure E.4, correlation between propionic acid weight percentage and the area under refractive index signal.

$$wt.\,\% = 1.185\ 10^{-8}\ X_{area} - 0.0001 \qquad (R^2 = 0.999) \tag{E-4}$$

E.5 Butyric acid calibration line

Table E.6, HPLC results from the reference mixture samples.

Weight concentration of acetic acid (wt. %)	Average of area
0.25%	214597.8
0.50%	465167.2
0.75%	644420.7
1.00%	954704.3
1.25%	1163379.8

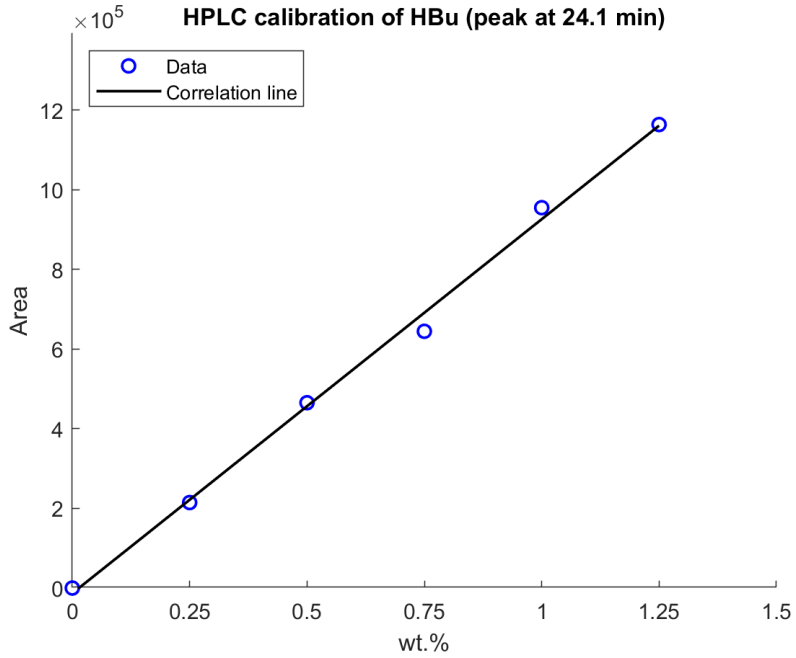

Figure E.5, correlation between butyric acid weight percentage and the area under refractive index signal.

$$wt.\% = 1.0612\ 10^{-8}\ X_{area} - 0.0002 \qquad (R^2 = 0.996) \qquad \text{(E-5)}$$

Appendix F: IC calibration lines

Ion chromatography is used next to HPLC to thoroughly analyse the adsorptive capacity of impregnated and non-impregnated resins when used to treat fermented wastewater. This analytical method is applied to measure the weight percentage of dissociated ions before and after the adsorption experiment. For this reason, calibration curves are produced for ions that are commonplace in fermented wastewater. The ion chromatography equipment has a sensible measurement range, and accurate measurements are possible when the analyte concentration is within the 20 - 220 ppm range. Therefore, a dilution step is required to analyse the weight percentage of compounds with a higher concentration.

The equipment can analyse samples with a higher than 5 ml volume. For the relevant cations and anions shown in Table F.1, calibration lines are produced by analysing reference samples made from standard solutions with a precise concentration of 1000 ppm.

The cations and anions that are relevant to the adsorption study of fermented wastewater are the following:

Table F.1, Cations and anions relevant to the study of adsorption in treatment of fermented wastewater

Cations	Anions
K^+, Na^+	$Cl^-, SO_4^{-2}, PO_4^{-3}$

The corresponding specification of diluted samples made from the standard solutions is provided in Table F.2. In the following next subsections, the corresponding calibration line, graphical representation, and explicit correlation of each of the ions are provided to the reader.

Table F.2, reference samples used in producing the calibration lines.

Volume of std sol (µl)	Volume of mili-q water (ml)	ppm
310	10	30
810	10	75
1364	10	120
1976	10	165
2658	10	210

F.1 Sodium cation IC calibration line

Table F.3, IC results from the reference samples of sodium cation (retention time = 7.3 min)

Concentration of sodium cation (ppm)	Average of area ($\frac{\mu S}{cm} min$)
30	10583
75	22359
120	37562
165	50573
210	64052

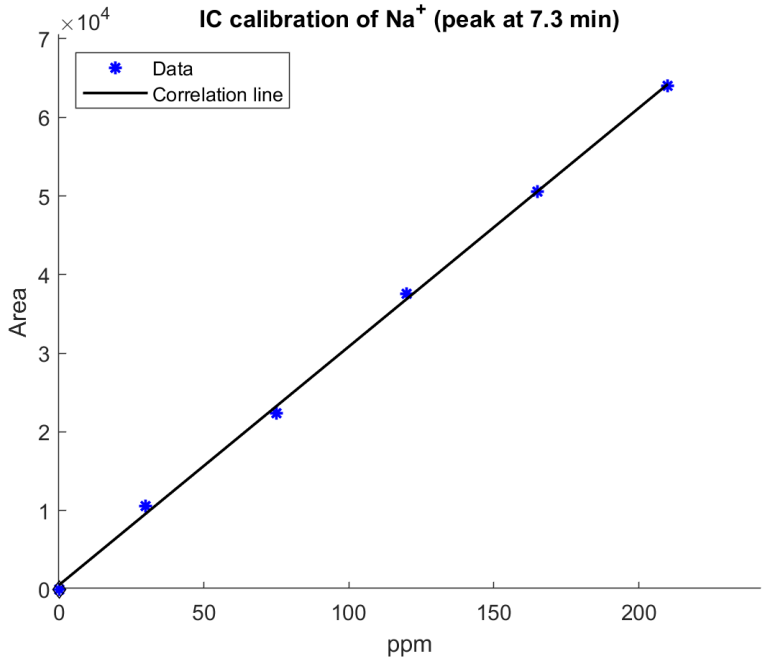

Figure F.1, correlation between sodium cation concentration and the area under peak at 7.3 min.

$$ppm = 0.003293\ X_{area} - 1.614 \qquad (R^2 = 0.999) \tag{F-1}$$

F.2 Potassium cation IC calibration line

Table F.4, IC results from the reference samples of potassium cation (retention time = 11.6 min)

Concentration of potassium cation (ppm)	Average of area ($\frac{\mu S}{cm} min$)
30	4.922
75	12248
120	19780
165	26493
210	34240

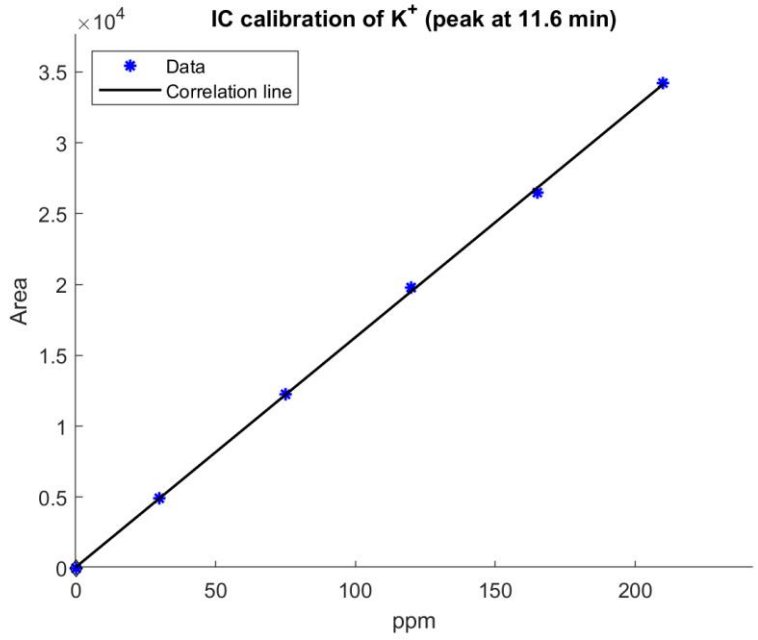

Figure F.2, correlation between potassium cation concentration and the area under peak at 11.6 min.

$$ppm = 0.006161\, X_{area} - 0.3051 \qquad (R^2 = 0.999) \qquad \text{(F-2)}$$

F.3 Sulphate anion IC calibration line

Table F.5, IC results from the reference samples of sulphate anion (retention time = 15.3 min)

Concentration of sulphate anion (ppm)	Average of area ($\frac{\mu S}{cm} min$)
30	7395
75	18431
120	28901
165	38506
210	49069

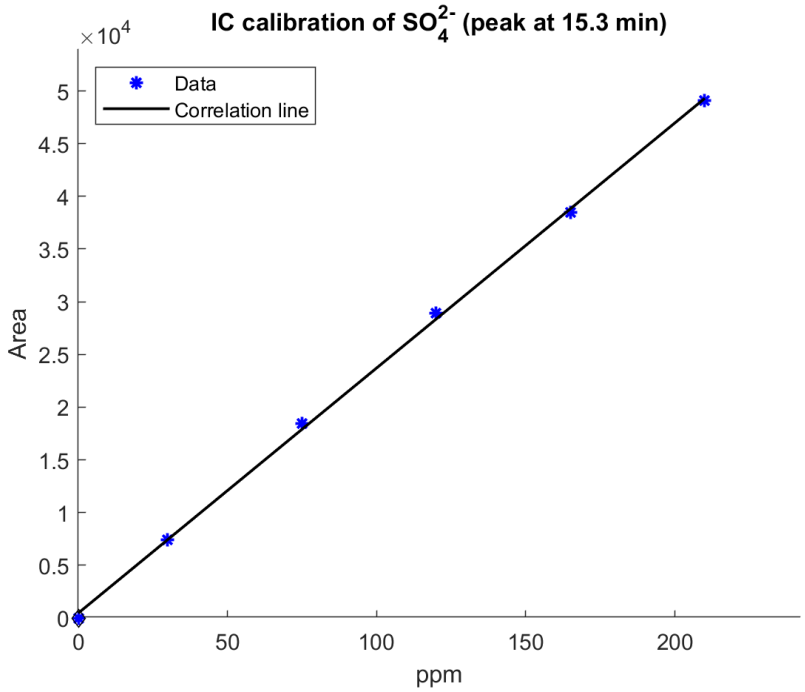

Figure F.3, correlation between sulphate cation concentration and the area under peak at 15.3 min.

$$ppm = 0.004298\, X_{area} - 1.927 \quad (R^2 = 0.999) \tag{F-3}$$

F.4 Chloride anion IC calibration line

Table F.6, IC results from the reference samples of chloride anion (retention time = 5.4 min)

Concentration of chloride anion (ppm)	Average of area ($\frac{\mu S}{cm} min$)
30	9979
75	24625
120	38429
165	51151
210	66254

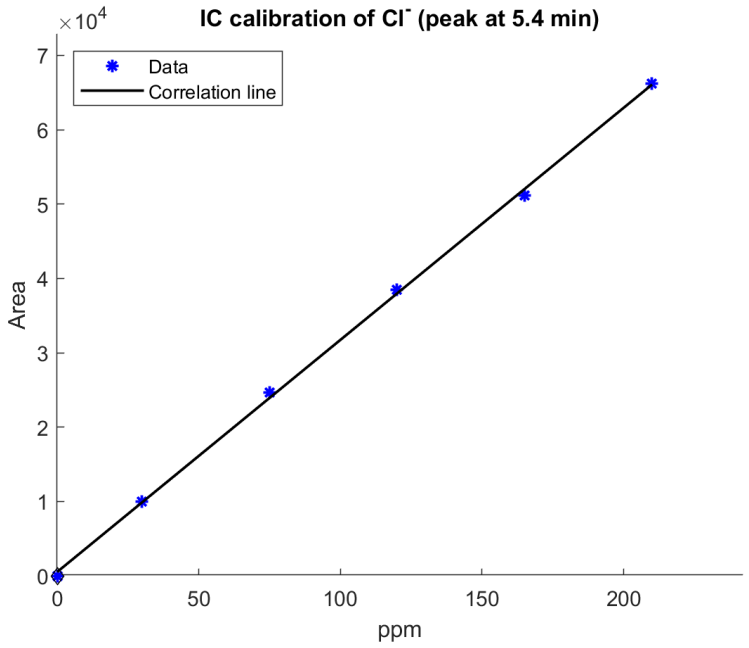

Figure F.4, correlation between chloride anion concentration and the area under peak at 5.4 min.

$$ppm = 0.003201 X_{area} - 1.620 \quad (R^2 = 0.999) \qquad \text{(F-4)}$$

F.5 Phosphate anion IC calibration line

Table F.7, IC results from the reference samples of phosphate anion (retention time = 17.7 min)

Concentration of phosphate anion (ppm)	Average of area ($\frac{\mu S}{cm} min$)
30	1616
75	5271
120	8807
165	13340
210	17896

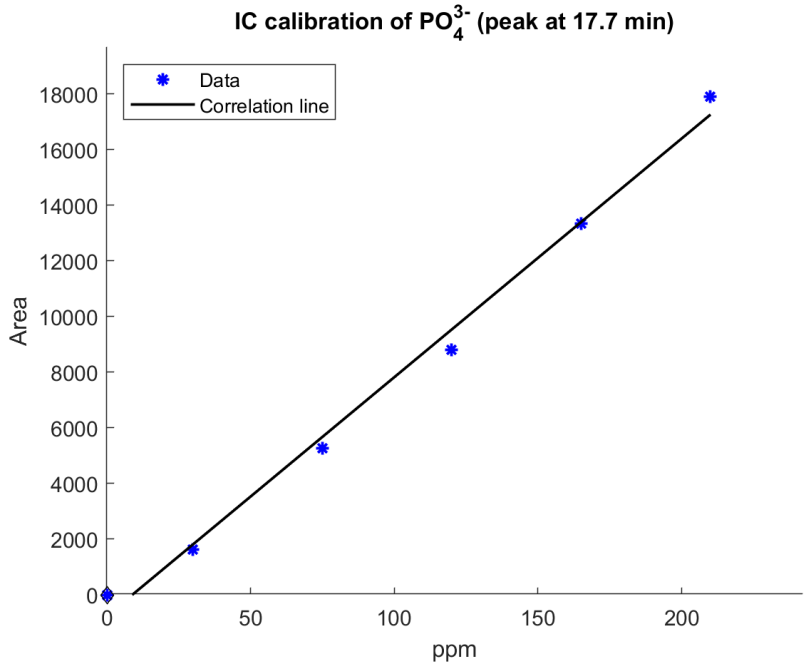

Figure E.5, correlation between phosphate anion concentration and the area under peak at 17.7 min.

$$ppm = 0.01157\, X_{area} + 9.490 \quad (R^2 = 0.9928) \tag{F-5}$$

Appendix G: Calibration line for AAS of iron content

As mentioned in Chapter 3, the mass of MNP diffused into the resins is evaluated using atomic absorption spectroscopy. For this analysis, a 30 mg sample is digested in 2.4 ml of highly concentrated acid (1.8 ml of hydrochloride wt. 36% and 0.6 ml of nitric acid wt. 69%). The acid solution is further diluted with milli-q water. The dilution is done by adding 1 ml to 40 ml of milli-q water. The dilution of the sample is necessary for two reasons. First, the sample must be filtered using a syringe with a microcap. Highly concentrated acids can dissolve the needle during intake, thus, introducing error. Additionally, the instrument has been calibrated to measure iron contents below 100 ppm. The calibration line for this instrument is graphically represented in Figure G.1

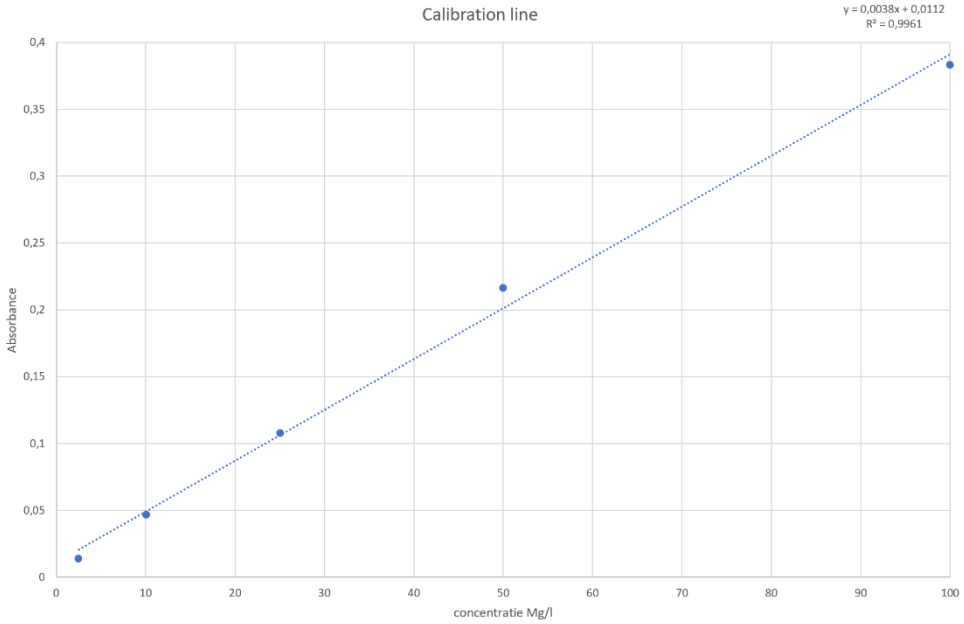

Figure G.1, Calibration line for iron content in AAS.

$$X_{abs} = 0.0038\,PPM + 0.0112 \quad (R^2 = 0.9961) \tag{G-1}$$